Instability analysis of the split-step Fourier method on the background of a soliton of the nonlinear Schrödinger equation

T.I. Lakoba[*]

August 22, 2010

Abstract

We analyze a numerical instability that occurs in the well-known split-step Fourier method on the background of a soliton. This instability is found to be very sensitive to small changes of the parameters of both the numerical grid and the soliton, unlike the instability of most finite-difference schemes. Moreover, the principle of "frozen coefficients", in which variable coefficients are treated as "locally constant" for the purpose of stability analysis, is strongly violated for the instability of the split-step method on the soliton background.

Our analysis quantitatively explains all these features. It is enabled by the fact that the period of oscillations of the unstable Fourier modes is much smaller than the width of the soliton. Our analysis is different from the von Neumann analysis in that it requires spatially growing or decaying harmonics (not localized near the boundaries) as opposed to purely oscillatory ones.

Keywords: Split-step Fourier method, Numerical instability, Nonlinear evolution equations, Solitary waves.

Mathematics Subject Classification (2000): 65M12, 65M70.

---

[*]Department of Mathematics and Statistics, 16 Colchester Ave., University of Vermont, Burlington, VT 05401, USA (`lakobati@cems.uvm.edu`).

1   Introduction

The split-step Fourier method is widely used in numerical simulations of nonlinear wave equations. In particular, it is the mainstream method in nonlinear optics, where the fundamental equation describing propagation of an electromagnetic pulse or beam is the nonlinear Schrödinger equation

$$iu_z - \beta u_{tt} + \gamma u|u|^2 = 0\,, \qquad u(t,0) = u_0(t). \tag{1.1}$$

In this paper, we use notations adopted in fiber optics [1], whereby u is proportional to the complex envelope of the electric field, z is the propagation distance along the fiber, and t is the time in the reference frame moving with the pulse. (The subscripts denote partial differentiation.) Thus, z and t are the evolution and spatial variables, respectively. Also, in Eq. (1.1), β and γ are proportional to the group velocity dispersion and nonlinear refractive index of the optical fiber, respectively. Although these real-valued constants can be scaled out of the equation by an appropriate nondimensionalization, we will keep them in our analysis to distinguish contributions of the dispersive and nonlinear terms. Solitons with $u(z, |t| \to \infty) \to 0$ exist in (1.1) for $\beta\gamma < 0$.

The idea of the split-step method is the following. Equation (1.1) can be solved analytically when only one of the dispersive and nonlinear terms is nonzero. Then, the approximate numerical solution of (1.1) can be obtained in a sequence of steps which alternatingly account either for the dispersion or for the nonlinearity:

$$\begin{aligned} &\text{for } n \text{ from } 1 \text{ to } n_{\max} \text{ do:} \\ &\quad u_{\mathrm{nonlin}}(t) = u_n(t)\,\exp\left(i\gamma|u_n(t)|^2\Delta z\right) \\ &\quad u_{n+1} = \mathcal{F}^{-1}\Big[\exp(i\beta\omega^2\,\Delta z)\,\mathcal{F}\big[u_{\mathrm{nonlin}}(t)\big]\Big] \\ &\text{end} \end{aligned} \tag{1.2}$$

Here Δz is the step size along the evolution variable, and the subscript n now denotes the value at the nth step[1]. In algorithm (1.2), the evolution due to the dispersive term is computed using the Fourier transform $\mathcal{F}$ and its inverse $\mathcal{F}^{-1}$, where, e.g.:

$$\mathcal{F}[u](\omega) = \int_{-\infty}^{\infty} u(t)e^{-i\omega t}dt\,. \tag{1.3}$$

For equations of the form (1.1), such an algorithm was originally applied in [2] – [4] and later comprehensively studied in [5]. Implementations where the dispersive term is computed using finite-difference discretization in t can be used as well, but the Fourier-based implementation is preferred in optics, not only because of its higher accuracy (exponential versus algebraic in Δt for smooth pulses), but also because it allows one to easily handle more complicated dispersive terms than in (1.1). In this paper, we specifically focus on the Fourier-based implementation (1.2) of the split-step method.

---

[1]Using subscripts to denote iteration steps, as in (1.2), and partial differentiation, as in (1.1), will not lead to confusion.

Since the split-step method is explicit, one expects it to be only conditionally stable. However, the standard von Neumann stability analysis on the background of the trivial solution $u(t) = 0$ does not reveal any instability. Weideman and Herbst [6] were the first to rigorously show that the split-step method is indeed conditionally stable, with the instability being able to develop over the background of a *finite-amplitude* monochromatic wave

$$u_{\text{cw}} = A \exp(iKz - i\Omega_{\text{cw}}t), \qquad K = \beta\Omega_{\text{cw}}^2 + \gamma|A|^2, \quad A = \text{const.} \qquad (1.4)$$

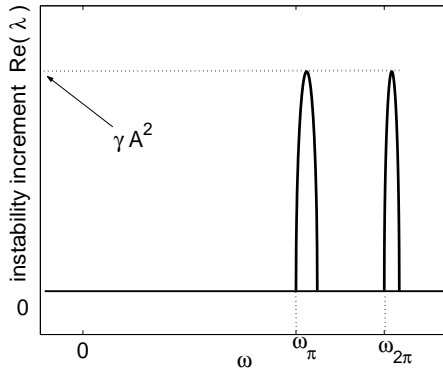A few years later, Matera et al [7] obtained a similar result by a more heuristic method.

Figure 1: Schematics of the numerical instability increment of method (1.2) over the background of a monocromatic wave (1.4) as a function of frequency ω. Only the part for $\omega > 0$ is shown, since the graph is symmetric about $\omega = 0$. The width of the instability peak near $\omega_{k\pi}$, where $k = 1, 2, \ldots$, equals $|\gamma A^2/(\beta\omega_{k\pi})|$ (see Appendix 3). Note that the case corresponding to $\beta < 0$ is shown; in the case of $\beta > 0$, the peaks will occur on the opposite sides of ω_π and $\omega_{2\pi}$.

The numerical instability increment of the split-step method of Eq. (1.1) with the background solution $\bar{u} \equiv u_{\text{cw}}$ (1.4), found by Weideman and Herbst, is schematically shown in Fig. 1 for a particular case of $\Omega_{\text{cw}} = 0$. (The formulae describing the location and growth rate of unstable modes are given in Appendix 3.) Here the notations are the following. The numerical solution of (1.1) is assumed to have the form

$$u_n = \bar{u} + \tilde{u}_n, \qquad |\tilde{u}_n| \ll |\bar{u}|, \qquad (1.5a)$$

$$\tilde{u}_n = \tilde{A}\exp(\lambda z_n - i\omega t), \qquad z_n = n\Delta z, \quad \omega = \frac{2\pi\ell}{T}, \qquad (1.5b)$$

where $-T/2 \leq t \leq T/2$ and the limits for the integer index ℓ are determined by the number of grid points. In Fig. 1,

$$\omega_\pi = \sqrt{\frac{\pi}{|\beta|\,\Delta z}}, \qquad \text{i.e.} \quad |\beta|\omega_\pi^2\Delta z = \pi, \qquad (1.6)$$

3

and, similarly, $|\beta|\omega_{2\pi}^2 \Delta z = 2\pi$. Instability peaks of the same height exist also near $\pm\omega_{3\pi}$, as long as $\omega_{\max} \equiv \pi/\Delta t$, where Δt is the mesh size along t, extends beyond $\omega_{3\pi}$; etc.

Note that the instability depicted in Fig. 1 is mild, in the sense that the numerical error grows by a factor $\exp\big(O(1)\big)$ over propagation distances of order $O(1)$. Furthermore, this instability remains mild even when Δz significantly exceeds its threshold

$$\Delta z_{\text{thresh}} \approx \frac{\pi}{|\beta|\omega_{\max}^2} \tag{1.7}$$

(see (1.6)). This should be contrasted with the behavior of finite-difference explicit schemes, e.g., the Runge–Kutta scheme for the Heat equation, where the instability becomes strong (i.e. the numerical error grows by a factor of $\exp\big(O(1)\big)$ over propagation distances of only $O(\Delta z)$) whenever the step size along the evolution variable exceeds the instability threshold. Another remarkable property of the instability in Fig. 1 is that it occurs only in a finite (and rather narrow, of width $O(\gamma A^2/(|\beta|\omega_\pi) = O(\sqrt{\Delta z}))$) band of spatial frequencies ω, whereas instabilities of other explicit schemes occur, typically, for *all* frequencies higher than a certain minimum value. Let us note a curious consequence of this spectral selectivity of the instability of the split-step method: The method can be found stable even when Δz exceeds the threshold (1.7). This can occur when the width of the instability peak is less than the mesh size $\Delta\omega$ in the frequency domain [6]; see also Appendix 3.

In this paper, we will show, first via numerical simulations and then by an analytical calculation, that the properties of the instability of the split-step Fourier method on the background of a soliton solution are considerably different from properties of such instability on the monochromatic wave background. In particular, these new properties are even more distinct from some propeties of instabilities of well-known finite-difference explicit schemes. Highlights of these new properties include: high sensitivity to (i) the step size Δz and (ii) the length T of the time window (recall that time t in (1.1) is the spatial coordinate), and also (iii) a violation of the so called principle of "frozen coefficients" (see below). Property (i) has been considered both numerically and analytically for the monochromatic wave background, and numerically for the soliton background, in [8]. We will explain later on that this property, i.e. the high sensitivity of the instability to the step size Δz, has different dependence on the time window length T, and also requires a different mathematical description, for the monochromatic and soliton backgrounds. As for properties (ii) and (iii), they, to the best of our knowledge, have not been previously systematically studied for any numerical scheme.

In Section 2, we will present results of our numerical simulations of Eq. (1.1) by the split-step Fourier method (1.2) on the background of the soliton

$$u_{\text{sol}} = A\sqrt{\frac{2}{\gamma}}\,\text{sech}\left(\frac{A\,t}{\sqrt{-\beta}}\right)\exp\left(iKz\right) \equiv U(t)e^{iKz}, \qquad K = A^2. \tag{1.8}$$

These will illustrate the unusual instability properties listed in the previous paragraph. In Section 3, we will develop an analytical theory of the instability of the slit-step Fourier method on the background of the soliton which explains all these observed propeties. A comparison of this theory with numerical simulations is presented in Section 4. In Section 5 we extend our analysis to higher-order versions of the split-step method. In Section 6 we summarize this work. Appendices 1 and 2 contain auxiliary results, and Appendix 3 recovers the results of Weideman and Herbst [6], illustrated in Fig. 1, via the analytical method presented in Section 3.

2 Numerical study of the instability of the split-step Fourier method on the background of a soliton

We numerically simulated Eq. (1.1) with $\beta = -1$, $\gamma = 2$ on the background of the soliton (1.8) with $A = 1$ using algorithm (1.2). We added to the initial soliton a very small white (in t) noise component, which served to reveal unstable Fourier modes sooner than if they had developed from the round-off error. Thus, the initial condition for our numerical experiments was

$$u_0(t) = A \operatorname{sech}(At) + \xi(t), \qquad A = 1, \tag{2.1}$$

and $\xi(t)$ was a Gaussian random process with zero mean and the standard deviation 10^{-10}.

To begin, we considered the spatial grid $-T/2 < t \leq T/2$ with 2^{10} grid points and width $T = 32\pi$, i.e. about two orders of magnitude wider than the soliton. This results in the spectral grid being the interval $-32 < \omega \leq 32$ with the frequency spacing of $\Delta\omega = 2\pi/T = 0.0625$. As expected, we did not observe any instability for $\Delta z < \Delta z_{\text{thresh}} \approx 0.0031$. Above the threshold, we ran the simulations with Δz ranging from 0.004 to 0.006 with the increment of 0.0001 (i.e., $\Delta z = 0.0040, 0.0041, \ldots 0.0060$) up to the maximum distance of $z_{\max} = 500$ and observed instability only at a few values of Δz listed in Table 1. A typical Fourier spectrum of the unstable solution at $z_{\max}$ is illustrated in Fig. 2 for $\Delta z = 0.0040$. The instability increment (see (1.5b)) listed in Table 1 was computed as

$$\operatorname{Re}(\lambda) = \frac{(\text{peaks' exponent}) - (\text{noise's exponent})}{z_{\max}} \ln 10, \tag{2.2}$$

where the peaks's exponent refers to the average of the decimal exponents of the two peaks in Fig. 2(b), and the exponent corresponding to the average noise level was estimated to be -8.8 for this set of simulations. Estimate (2.2) may not be very accurate, as the so computed increment depends on the noise levels at the frequencies

Δz	$\omega_{\text{left}}^{(+)} - \omega_\pi$	ω_π	$\omega_{\text{right}}^{(+)} - \omega_\pi$	$\text{Re}(\lambda)$
0.0040	-0.72	28.03	0.66	0.019
0.0048	-0.39	25.58	0.35	0.031
0.0054	-0.62	24.12	0.57	0.022
0.0055	-0.52	23.90	0.48	0.024
0.0058	-0.46	23.27	0.42	0.022

Table 1: Parameters of the unstable frequencies' peaks when $T = 32\pi$, number of grid points is 2^{10}, and Δz is varied as 0.0040, 0.0041, 0.0042, ... , 0.0060. The notations $\omega_{\text{right, left}}^{(+)}$ are introduced in Fig. 2.

of the unstable Fourier modes (hence the peaks in Fig. 2 are slightly different), but it still provides a reasonable measure of the instability rate.

¿From Fig. 2 we first observe that the instability peaks at negative frequencies are not reflectionally symmetric relative to such peaks at positive frequencies, in contrast to the instability peaks on the background of a monochromatic wave (see the caption to Fig. 1). Rather, for all the simulations we ran, the negative-frequency peaks appear to be a *shifted* replica of the positive-frequency peaks. Moreover, the frequencies of the left and right peaks on the same side of $\omega = 0$ are slightly asymmetric with respect to ω_π: see Table 1. To further investigate how the peaks are related to one another, we ran a simulation where we placed a narrow filter that totally suppressed the field around $\omega = \omega_{\text{right}}^{(+)}$. As a result, the peak at $\omega = \omega_{\text{right}}^{(-)}$ was suppressed but the peaks at $\omega = \omega_{\text{left}}^{(\pm)}$ remained intact. This corroborated the aforementioned observation that the pairs of peaks appear to be shifted replicas of each other rather than reflected about $\omega = 0$. In light of this, it might be somewhat surprising that the peak's frequencies are found to be related by a reflectional symmetry:

$$\omega_{\text{left}}^{(-)} = -\omega_{\text{right}}^{(+)}, \qquad \omega_{\text{right}}^{(-)} = -\omega_{\text{left}}^{(+)}. \tag{2.3}$$

All these observations are explained by the theory in Section 3.

Another conspicuous observation, made from Table 1, is that there seems to be no apparent order in the frequencies and heights of the instability peaks as functions of Δz. To expand on this, we zoomed in on the interval $0.0045 \leq \Delta z \leq 0.0046$, at the end points of which we had found *no* instability. We varied $\Delta z = 0.00451, 0.00452, \ldots 0.00459$ and found that the instability occured at $\Delta z = 0.00451$ and persisted up to $\Delta z = 0.00456$, with its increment $\text{Re}(\lambda)$ gradually decreasing from 0.036 to 0.014 and the inter-peak spacing $\omega_{\text{right}}^{(+)} - \omega_{\text{left}}^{(+)}$ gradually increasing from 0.25 to 1.56. A weaker instability, with the inter-peak spacing of about 2.0, was also observed at $\Delta z = 0.00459$; note that no instability was observed at $\Delta z = 0.00457$ and 0.00458.

One could argue that such an irregular dependence of the instability on Δz occurs simply because the width of the band of unstable modes is just slightly greater than
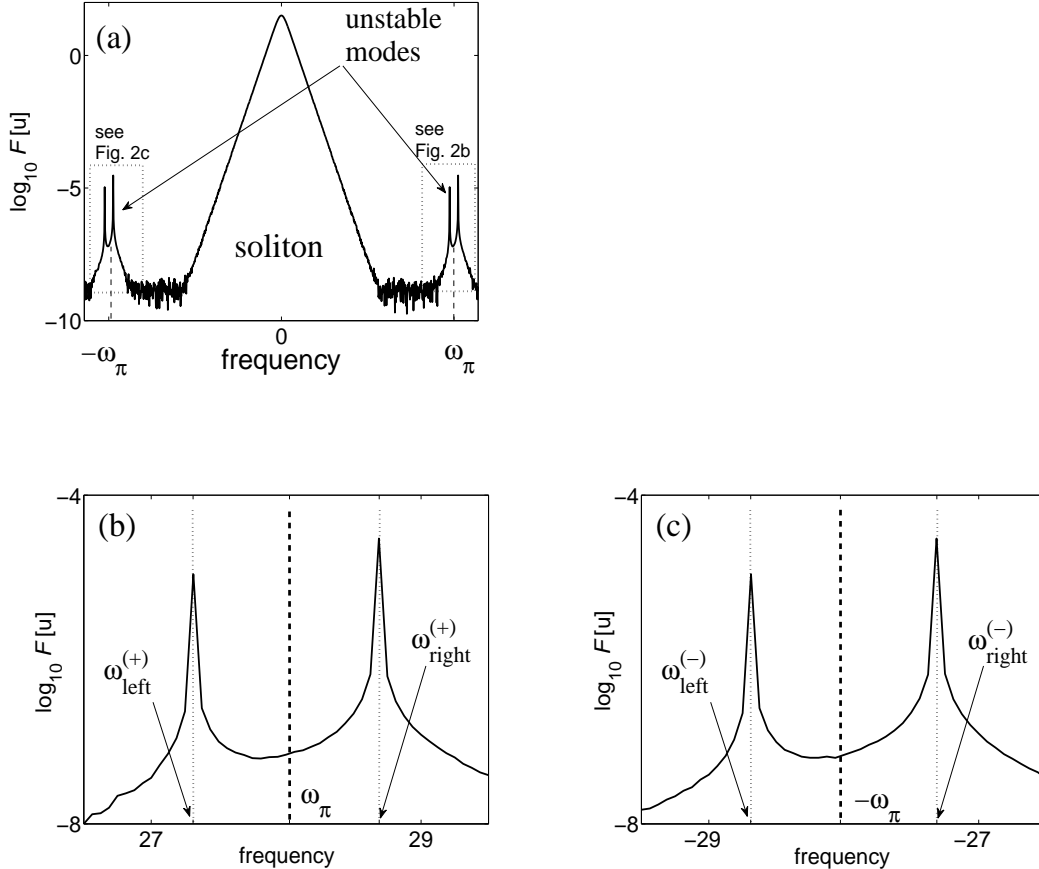
Figure 2: The spectrum of the solution of (1.1) and (2.1) at $z = 500$ with $\Delta z = 0.0040$, computed by method (1.2). Other parameters are listed in the text after Eq. (2.1).

the mesh size $\Delta\omega$ of the frequency grid. Indeed, the unstable band's width estimated from the monochromatic-background case is $\gamma A^2/(|\beta|\omega_\pi) \approx 0.07$ for the parameters listed above (see the caption to Fig. 1 and formula (A3.6) in Appendix 3), while $\Delta\omega \equiv 2\pi/T = 0.0625$. In such a case, the instability features should be strongly sensitive to where inside the instability band the frequency $2\pi\ell/T$ falls. This was pointed out in [8]; see also the end of Appendix 3 below. Then one would expect that the aforementioned sensitivity is to be alleviated by taking a wider time window, because then the frequency mesh size $\Delta\omega$ would decrease and more frequencies from the numerical grid would fall into the unstable band.

To verify the validity of such an argument, we re-run the simulations described above taking a four times wider time window, i.e. $T = 128\pi$, while retaining the same Δt (thus quadrupling the number of grid points). For these new simulations, we estimate that instability peaks should contain about four grid points and hence may expect that the high sensitivity to the value of Δz reported above is to be alleviated. What we find instead is *an opposite* of this statement: the dependence of the locations and heights of the instability peaks remains at least as irregular as for the smaller value of
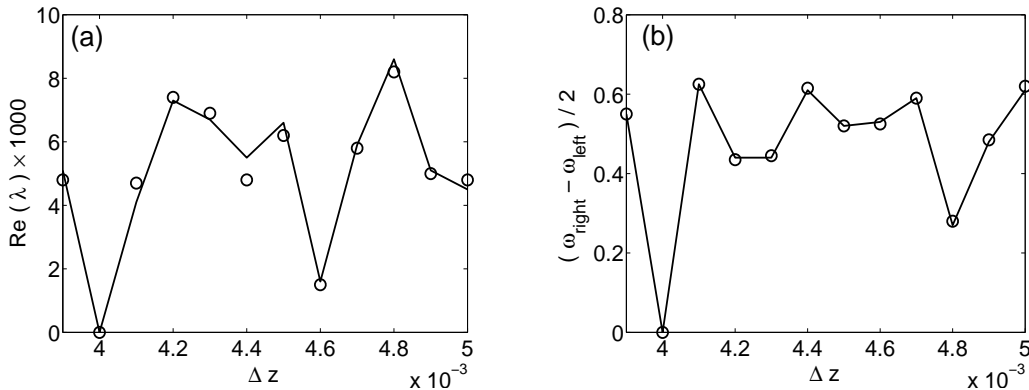
Figure 3: Instability increment and unstable peaks' half-separation at $z = 2000$, as a function of the step size Δz. The initial condition is (2.1). The numerical domain has length $T = 128\pi$ and contains 2^{12} grid points. Note that for $\Delta z = 0.0040$, where no instability is found, we *defined* the corresponding $\omega_{\text{right}} - \omega_{\text{left}} = 0$. The open circles and solid line correspond, respectively, to the numerical results and to the results of analytical calculations reported in Section 4.2.

T, but now the instability is observed "more often" than in Table 1. In Figs. 3 and 4 we plot the observed values of the instability increment and half of the inter-peak spacing, $(\omega_{\text{right}}^{(+)} - \omega_{\text{left}}^{(+)})/2$, when Δz is varied between 0.0039 and 0.0050 with step 0.0001 and between 0.00471 and 0.00479 with step 0.00001. Since the instability rates have now been found to be about a factor of four lower than in Table 1, we had to run our simulations up to a greater distance, $z_{\max} = 2000$. Note that the instability characteristics reported for $0.0040 \leq \Delta z \leq 0.0050$ in Table 1 do *not* match those shown in Fig. 3. Moreover, we find that the spectra of unstable modes may look qualitatively different than in Fig. 2. Namely, these spectra for $\Delta z = 0.0044$, 0.0045, 0.00474, 0.0049, look like the one shown in Fig. 5(a), while for $\Delta z = 0.0050$ it is shown in Fig. 5(b). Also, contrary to our expectation, we observe that in most cases the instability peaks still contain only one grid point; exceptions are the central peak for $\Delta z = 0.0050$ and the peaks for $\Delta z = 0.00478$, which are spaced very closely. This fact will be emphasized when we describe a challenge in the analytical description of the instability in Section 3.

We have already mentioned that keeping the spatial mesh size Δt intact but increasing the spatial window's length T by a factor of four considerably changes parameters of the instability. We now show that just *slightly* changing T (and hence correspondingly slightly changing Δt) may change instability parameters *dramatically*. Such a sensitivity to the length of the spatial window is not observed for finite-difference methods. Note that $T = 128\pi \approx 402.1$. In Table 2 we list the instability parameters observed when we decrease T by about 1% or even less. Again, these results appear to be totally
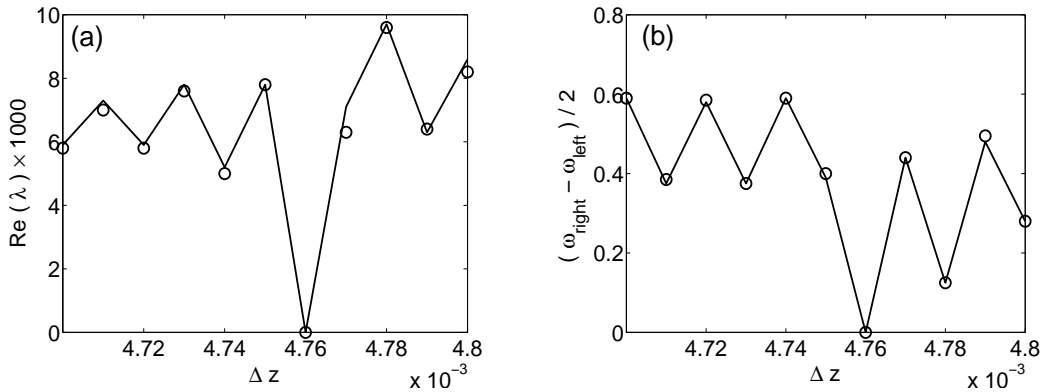
Figure 4: Same as in Fig. 3, but for a different interval of Δz values.
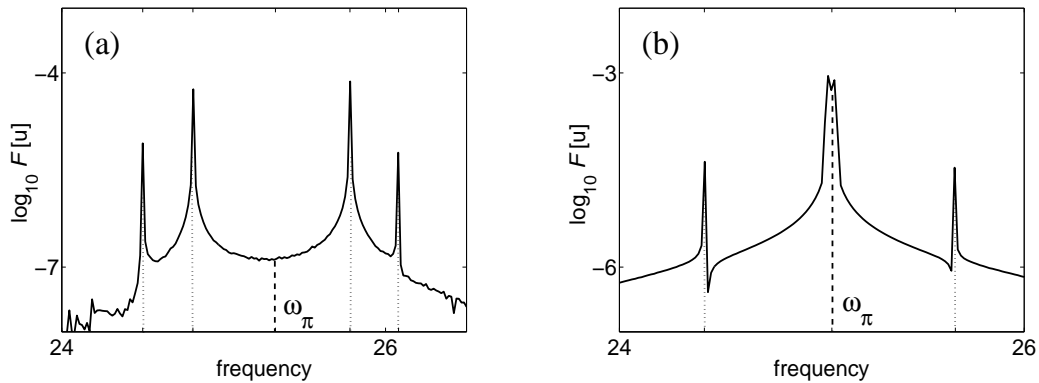

Figure 5: "Less typical" instability spectra. Both panels are for initial condition (2.1), the propagation distance $z = 2000$, and the numerical domain with $T = 128\pi$ and 2^{12} grid points. (a) $\Delta z = 0.0049$; similar spectra are found for $\Delta z = 0.0044, 0.0045, 0.00474$; (b) $\Delta z = 0.0050$.

irregular. Similarly to the situation mentioned at the end of the previous paragraph, only the closely spaced instability peaks at $T = 398$ contain several grid points; the peaks for the other values of T each contain only one grid point.

Finally, let us show that the so called principle of "frozen coefficients" [9], which is known to apply to finite-difference schemes, does *not* hold for the split-step Fourier method (1.2) on the background of a soliton. This principle says the following. Suppose one has an evolution equation with a spatially varying coefficient, say $c(t)$ (recall that in this paper, t is the spatial variable, while z is the evolution variable). Near each $t = t_0$, this coefficient can be approximated by $c(t_0)$. Then one can apply the standard von Neumann stability analysis to the equation with the *constant* ("frozen") coefficient $c(t_0)$. Then the scheme is deemed unstable if such an analysis reveals insta-

9

T	$\omega_{\text{left}}^{(+)} - \omega_\pi$	$\omega_{\text{right}}^{(+)} - \omega_\pi$	$\text{Re}(\lambda)$
397	-0.44	0.40	0.0062
398	-0.10	0.08	0.0096
399	-1.09	1.02	0.0024
400	-0.33	0.29	0.0076
128π	-0.39	0.36	0.0076

Table 2: Parameters of the unstable frequencies' peaks when $\Delta z = 0.0043$ ($\omega_\pi = 27.03$), number of grid points is 2^{12}, and T is varied.

bility for at least one value of $c(t_0)$. This principle works quite well for finite-difference schemes. An intuitive explanation fot this is that the unstable modes usually have high spatial frequency, and so they "see" a relatively slowly-varying coefficient $c(t)$ as being approximately constant near each $t = t_0$. For the split-step Fourier method, the unstable modes also have high spatial frequencies, $\approx \pm\omega_\pi$. Yet, the principle of "frozen coefficients" does not apply to this method, as we illustrate below.

One manifestation of this fact, as we have already seen, is that the instability of method (1.2) on the background of a soliton is different from that on the background of a monochromatic wave of the same amplitude. This observation was originally made by Weideman and Herbst, who, however, did not provide any details about it (see the last section in [6]). Now we will present three examples that deal with a multi-soliton background. Conclusions from these examples are at odds with our intuition based on the experience with finite-difference schemes, and they reveal yet another way in which the principle of "frozen coefficients" is violated for method (1.2). As at the beginning of this Section, let us use the numerical domain with $T = 32\pi \approx 100.5$ and 2^{10} grid points, but instead of the *single*-soliton initial condition (2.1), consider three *well-separated* solitons:

$$u_0(t) = \text{sech}\,(t + 33.5) + \text{sech}\,(t) + \text{sech}\,(t - 33.5) \, + \, \xi(t), \tag{2.4}$$

where $\xi(t)$ is the same as in (2.1). The spacing between the solitons is chosen to be sufficiently large so as to avoid their interaction. According to the principle of "frozen coefficients", the instability with this initial condition must be the same as with (2.1). However, it turns out to be quite different. First, for $\Delta z = 0.0040$, when there was an instability (see Table 1) for the initial condition (2.1), there is *no* instability for initial condition (2.4). Second, for $\Delta z = 0.0052$, when there was *no* instability according to Table 1, now there is a strong instability with the increment of about 0.10 (i.e., more than three times greater than the largest increment in Table 1). Third, for $\Delta z = 0.0058$, the instability was observed with both initial conditions (2.1) and (2.4), but for the latter case it was more than three times as strong (having the increment of 0.072).

To summarize, in this Section we have presented results of numerical simulations of the split-step Fourier method (1.2) with soliton initial conditions. These results illustrate the following features that are drastically distinct from features exhibited by unstable finite-difference schemes:

- The spectra of the unstable modes exhibit strong and irregular sensitivity to the values of the step size Δz and the length of the spatial window T;

- Instability on the background of several well-separated — and hence non-interacting — pulses can be drastically different from the instability on the background of a single pulse (or a different number of pulses).

The theory that we will present in the next section is able to *quantitatively* explain all these features.

3   Analytical theory of the instability of the split-step Fourier method on the background of a soliton

3.1   Key idea and main challenge

First, we will show that a straightforward application of the von Neumann analysis is unlikely to provide analytical insight about stability or instability of the split-step method on the soliton background. Then we will outline the idea of an alternative approach and point out the mathematical challenge that such an aproach would have to resolve.

Substituting expression (1.5a) with $\bar{u} = u_{\text{sol}}$ into algorithm (1.2) and keeping only terms linear in $\tilde{u}_n$, one obtains after taking the Fourier transform:

$$\mathcal{F}[\tilde{u}_{n+1}] = e^{i\beta\omega^2\Delta z} \, \mathcal{F}\left[e^{i\gamma|u_{\text{sol}}|^2\Delta z}\big(\tilde{u}_n + i\gamma\Delta z(u_{\text{sol}}^2\tilde{u}_n^* + |u_{\text{sol}}|^2\tilde{u}_n)\big)\right], \qquad (3.1)$$

where u_{sol} is given by (1.8). The right-hand side (r.h.s.) of (3.1) describes coupling of Fourier modes $\mathcal{F}[\tilde{u}_n](\omega_\ell)$ with different $\omega_\ell = 2\pi\ell/T$, $\ell = 0, \pm 1, \pm 2, \ldots$ via, e.g., the convolution term $\mathcal{F}\big[|u_{\text{sol}}|^2\tilde{u}_n\big]$, because $|u_{\text{sol}}|$ is a function of the spatial variable t. (Note that this problem did not occur in the stability analysis on the background of a monochromatic wave (1.4) since there $|\bar{u}| = |u_{\text{cw}}|$ is t-independent and hence the corresponding equation, studied by Weideman and Herbst, coupled only the modes ω_ℓ and $-\omega_\ell$.) Solving for eigenvalues of such a coupled multi-mode system, while numerically feasible, would unlikely provide any insight of how the instability can occur. Such an insight is provided by an alternative analytical approach described below.

The key idea of this approach comes from the instability spectra shown in Figs. 1, 2, and 5. Namely, we note that only narrow bands of Fourier modes with frequencies near $\pm\omega_\pi$ can become unstable. The reason for this will be presented later. Therefore, it is appropriate to seek the numerical error $\tilde{u}_n$, defined in (1.5a), as consisting of two quasi-monochromatic waves whose carrier frequencies are approximately $\pm\omega_\pi$. These waves can become unstable via their interaction mediated by their scattering on the soliton. Since these are high-frequency waves (see (1.6) and note that $\Delta z \ll 1$), they "see" the soliton, whose temporal width is $O(1)$, as a narrow, and hence small, perturbation. This is one of the reasons that the instability is weak, as seen in Section 2. Using the weakness of the instability, we will approximate its evolution by a differential, rather than difference, equation. Analysis of the former kind of equation is considerably easier than that of the latter one.

The main mathematical challenge that this approach needs to address is a *three-scale* nature of this problem, as can be seen from Fig. 2. One scale is set by $\omega_\pi \gg 1$, where the strong inequality is a consequence of $\Delta z \ll 1$ (see (1.6)), as is usually the case in simulations. Accordingly, let us define a small parameter

$$\epsilon = \frac{1}{\omega_\pi} \ll 1, \qquad \epsilon = O\left(\sqrt{\Delta z}\right), \tag{3.2}$$

which will play a prominent role in what follows. In addition to this $O(\epsilon^{-1})$ scale, there is also a scale $O(1)$: The separation between ω_π and the frequencies of the most unstable modes, seen as peaks in Fig. 2, appears to be of this order of magnitude. Finally, the third scale is set by the spectral width of the instability peaks. Indeed, as noted in Section 2, even for the highest spectral resolution reported there, those peaks, in most cases, contain only one grid point. (The pedestals seen around these peaks can be shown to occur due to modulational instability on the background of the peaks, i.e. are not directly caused by a numerical instability.) Based on the information provided by Figs. 2 and 5, it is even impossible to tell whether this third scale is determined by ϵ. We will show below that it is rather determined by several parameters of the problem. Incidentally, let us note that the instability on the background of a monochromatic wave has only two scales: the location $\pm\omega_\pi = O(\epsilon^{-1})$ of the instability peaks and the peaks' width, $O(\epsilon)$; see Fig. 1 and Appendix 3.

3.2 Details of the theory

Step 1: Derivation of a differential equation for the evolution of a numerical error $\tilde{u}_n$.

First, let us simplify the r.h.s. of (3.1) by noting that in practice, Δz is always taken so as to guarantee $\gamma|u_{\text{sol}}|^2\Delta z \ll 1$. Then, discarding terms $O\left((\gamma|u_{\text{sol}}|^2\Delta z)^2\right)$, one reduces (3.1) to

$$\mathcal{F}[\tilde{u}_{n+1}] = e^{i\beta\omega^2\Delta z}\, \mathcal{F}\left[\tilde{u}_n + i\gamma\Delta z(u_{\text{sol}}^2\tilde{u}_n^* + 2|u_{\text{sol}}|^2\tilde{u}_n)\right] . \tag{3.3}$$

Let us now use the observation made in the previous subsection: As follows from Figs. 1, 2, and 5, the instability occurs only in narrow spectral bands near $\pm\omega_\pi$, $\pm\omega_{2\pi}$, etc. We will focus on the instability near $\pm\omega_\pi$; the analysis near $\pm\omega_{2\pi}$ etc. is similar. (In Appendix 2 we will show that the instability can occur *only* near $\pm\omega_\pi$, $\pm\omega_{2\pi}$, etc., thereby recovering the results presented below.) Accordingly, let us rewrite (3.3) as

$$\mathcal{F}[\tilde{u}_{n+1}] = (-1) \cdot e^{i\beta(\omega^2 - \omega_\pi^2)\Delta z} \, \mathcal{F}\left[\tilde{u}_n + i\gamma\Delta z(u_{\mathrm{sol}}^2 \tilde{u}_n^* + 2|u_{\mathrm{sol}}|^2 \tilde{u}_n)\right] . \qquad (3.4)$$

where the (-1) in front of the r.h.s. occurs due to the definition of ω_π, Eq. (1.6). Note also that $\beta(\omega^2 - \omega_\pi^2)\Delta z = O(\epsilon)$, which follows from (3.2) and the fact that we consider frequencies satisfying $|\omega - (\pm\omega_\pi)| = O(1)$; see the end of Section 3.1. Thus, $\exp[i\beta(\omega^2 - \omega_\pi^2)\Delta z] = 1 + O(\epsilon) \approx 1$ for the frequencies of interest.

To enable further analysis of the still intractable difference equation (3.4) in the frequency domain, let us convert it into a partial differential equation in the time domain. To this end, we first observe that for the variable

$$\tilde{v}_n = (-1)^n \tilde{u}_n , \qquad (3.5)$$

Eq. (3.4) describes a *small* increment occurring from nth to $(n+1)$th step:

$$\mathcal{F}[\tilde{v}_{n+1}] = e^{i\beta(\omega^2 - \omega_\pi^2)\Delta z} \, \mathcal{F}\left[\tilde{v}_n + i\gamma\Delta z(u_{\mathrm{sol}}^2 \tilde{v}_n^* + 2|u_{\mathrm{sol}}|^2 \tilde{v}_n)\right] . \qquad (3.6)$$

Indeed, from (3.6) and the estimate $\exp[i\beta(\omega^2 - \omega_\pi^2)\Delta z] = 1 + O(\epsilon)$ it follows that $\tilde{v}_{n+1} - \tilde{v}_n = O(\epsilon)$. Accordingly, we define a *continuous* variable $\tilde{v}(z,t)$ which at $z_n = n\Delta z$ is related to $\tilde{u}_n$ by (3.5). Then, we show in Appendix 1 that a variable $\tilde{w} = \tilde{v}\,e^{-iKz}$ satisfies an equation

$$\tilde{w}_z = -i\beta(\tilde{w}_{tt} + \omega_\pi^2 \tilde{w}) - iK\tilde{w} + i\gamma U^2(\tilde{w}^* + 2\tilde{w}), \qquad (3.7)$$

where K and $U \equiv U(t)$ are defined in (1.8), and we have neglected terms of magnitude $O(\epsilon)$ (see Appendix 1). Note that the first group of terms on the r.h.s. of (3.7) has the order of magnitude $O(1/\epsilon)$ (see the text after (3.4)), and thus it describes waves rapidly oscillating in both z and t, as we have announced in Section 3.1.

Step 2: Approximate solution of Eq. (3.7).

We seek a solution of (3.7) as

$$\tilde{w} = p\,e^{-i\omega_\pi t} + m^*\,e^{i\omega_\pi t} , \qquad (3.8)$$

where $p(t,z)$ and $m(t,z)$ are assumed to vary in time on a scale $O(1)$. This agrees with the numerical observation in Section 2 that frequencies of unstable Fourier modes differ from $\pm\omega_\pi$ by $O(1)$ in most cases. Substituting (3.8) into (3.7) and separating terms proportional to $\exp(\pm i\omega_\pi t)$, one obtains:

$$p_z = -2(\beta/\epsilon)p_t - iKp - i\beta p_{tt} + i\gamma U^2(m + 2p), \qquad (3.9a)$$

13

$$m_z = 2(\beta/\epsilon)m_t + iKm + i\beta m_{tt} - i\gamma U^2(p + 2m), \qquad (3.9b)$$

where we have used definition (3.2). Using again the aforementioned numerical observation from Section 2, we seek solutions of (3.9) in the form

$$p = p_{\text{slow}}(\tau) \exp\left[-i\Omega t + 2i(\beta/\epsilon)\Omega z + \beta\Lambda z\right], \qquad (3.10a)$$

$$m = m_{\text{slow}}(\tau) \exp\left[i\Omega t + 2i(\beta/\epsilon)\Omega z + \beta\Lambda z\right], \qquad (3.10b)$$

where

$$\Omega = O(1) \qquad (3.11)$$

labels a particular Fourier mode of $\tilde{w}$, parameter Λ is to be determined later, and

$$\tau = \epsilon t, \qquad \Lambda \equiv \Lambda_R + i\Lambda_I. \qquad (3.12)$$

Note that $\beta\Lambda_R$ equals $\text{Re}(\lambda)$ in (1.5b). When writing that p_{slow} and m_{slow}, as well as $P(\tau)$ and $M(\tau)$ in (3.15) below, are functions of the "slow" time τ, we mean that

$$(p_{\text{slow}})_t, \ (m_{\text{slow}})_t, \ P_t, \ M_t \quad \text{are all of order } O(\epsilon). \qquad (3.13)$$

The order-of-magnitude estimate (3.11), which we empirically deduced from numerical experiments, will be generalized at the end of Section 4.

Let us stress that in ansatz (3.10), the p- and m-components of the solution are assumed to have *different* t-dependences on the $O(1)$ scale (due to the exponents $\pm i\Omega t$). As we show in Appendix 3, this assumption is one of the key steps that distinguishes the instability analysis on the soliton background from that on the monochromatic-wave background.

Next, substitution of (3.10) into (3.9) produces a pair of z-independent equations:

$$2(1 + \epsilon\Omega)(p_{\text{slow}})_\tau = \left(-iK/\beta + i\Omega^2 - \Lambda\right)p_{\text{slow}} + i(\gamma/\beta)U^2(\tau/\epsilon)\left(m_{\text{slow}}\,e^{2i\Omega\tau/\epsilon} + 2p_{\text{slow}}\right), \qquad (3.14a)$$

$$2(1 - \epsilon\Omega)(m_{\text{slow}})_\tau = \left(-iK/\beta + i\Omega^2 + \Lambda\right)m_{\text{slow}} + i(\gamma/\beta)U^2(\tau/\epsilon)\left(p_{\text{slow}}\,e^{-2i\Omega\tau/\epsilon} + 2m_{\text{slow}}\right). \qquad (3.14b)$$

In writing these equations we have neglected terms $O(\epsilon^2)$, which will be justified by subsequent calculations. Note also that the soliton background, $U^2(\tau/\epsilon)$, presents a *narrow* obstacle for $p_{\text{slow}}(\tau)$ and $m_{\text{slow}}(\tau)$. Since outside the soliton, p_{slow} and m_{slow} are not coupled to each other, we use yet another substitution:

$$p_{\text{slow}} = P \exp\left[\frac{i(-K/\beta + \Omega^2) - \Lambda}{2(1 + \epsilon\Omega)}\tau\right], \qquad (3.15a)$$

$$m_{\text{slow}} = M \exp\left[\frac{i(-K/\beta + \Omega^2) + \Lambda}{2(1 - \epsilon\Omega)}\tau\right]. \qquad (3.15b)$$

Then P and M change only in the vicinity of the soliton according to

$$P_\tau = \frac{i\gamma\,U^2(\tau/\epsilon)}{2\beta(1 + \epsilon\Omega)}\left(M\,e^{2i\Omega\cdot\tau/\epsilon + O(1)\cdot\tau} + 2P\right), \qquad (3.16a)$$

14

$$M_\tau = \frac{i\gamma\, U^2(\tau/\epsilon)}{2\beta(1-\epsilon\Omega)}\left(P\, e^{-2i\Omega\cdot\tau/\epsilon+O(1)\cdot\tau} + 2M\right). \tag{3.16b}$$

Integrating these equations over the entire time window $-\epsilon T/2 \le \tau \le \epsilon T/2$, one obtains:

$$P(+\epsilon T/2) - P(-\epsilon T/2) = i\epsilon\,\frac{\gamma}{2\beta}\left(\mathcal{F}[U^2](-2\Omega)\,M(0) + 2\mathcal{F}[U^2](0)\,P(0)\right), \tag{3.17a}$$

$$M(+\epsilon T/2) - M(-\epsilon T/2) = i\epsilon\,\frac{\gamma}{2\beta}\left(\mathcal{F}[U^2](2\Omega)\,P(0) + 2\mathcal{F}[U^2](0)\,M(0)\right). \tag{3.17b}$$

Here we have neglected terms $O(\epsilon^2)$ and used the definition (1.3) of the Fourier transform and the fact that the soliton is centered at $\tau = 0$. These relations prompt us to denote relative jumps ϵJ_P and ϵJ_M that P and M undergo across the soliton:

$$P(\pm\epsilon T/2) \equiv P(0)\,(1 \pm \epsilon J_P/2), \qquad M(\pm\epsilon T/2) \equiv M(0)\,(1 \pm \epsilon J_M/2). \tag{3.18}$$

Thus, by definition, $J_{P,M} = O(1)$. According to (3.17) and with the same accuracy, these jumps satisfy

$$J_P = i\,\frac{\gamma}{2\beta}\left(\mathcal{F}[U^2](-2\Omega)\,R + 2\mathcal{F}[U^2](0)\right), \tag{3.19a}$$

$$J_M = i\,\frac{\gamma}{2\beta}\left(\mathcal{F}[U^2](2\Omega)\,\frac{1}{R} + 2\mathcal{F}[U^2](0)\right), \tag{3.19b}$$

where $R = M(0)/P(0)$. Thus, the leading-order (in ϵ) approximate solution of Eqs. (3.9) can be obtained from (3.10), (3.15), (3.18), and (3.19). Qualitatively speaking, this solution is a superposition, (3.8), of fast-oscillating waves $p\,\exp[-i\omega_\pi t]$ and $m^*\exp[i\omega_\pi t]$, each of which experiences weak (due to $\epsilon \ll 1$) scattering on the soliton. The jumps of these fast-oscillating waves due to such scattering are determined by (3.19).

Step 3: Imposing the spatial periodicity condition.

Let us pause for a moment and recall what we are trying to do: We want to determine the instability increment $\beta\Lambda_R$ for the Fourier mode whose frequency is related to Ω by (3.10) and (3.8). The two equations (3.19) for three unknowns $J_{P,M}$ and R are insufficient for this purpose; note that they do not even involve Λ. The missing relations that will allow us to complete our task are supplied by the periodicity condition satisfied by $P(\tau)$ and $M(\tau)$ and are obtained as follows. First, note that the numerical error $\tilde{u}_n(t)$, and hence $\tilde{w}(t,z)$ defined before (3.6), satisfies periodic boundary conditions in t by virtue of the split-step method (1.2) using the discrete Fourier transform. Second, since $p(t,z)$ and $m^*(t,z)$ have different z-dependences (see (3.10)), then by virtue of (3.8) *each one* of these functions must satisfy periodic boundary conditions in t. Third, along with (3.8), (3.10), and (3.15), this implies that

$$\frac{P(+\epsilon T/2)}{P(-\epsilon T/2)} = \exp\left[\frac{i\left(K/\beta - \Omega^2\right) + \Lambda}{2(1+\epsilon\Omega)}\,\epsilon T + i(\omega_\pi + \Omega)T\right], \tag{3.20a}$$

15

$$\frac{M(+\epsilon T/2)}{M(-\epsilon T/2)} = \exp\left[\frac{i\left(K/\beta - \Omega^2\right) - \Lambda}{2(1 - \epsilon\Omega)}\,\epsilon T + i(\omega_\pi - \Omega)T\right]. \tag{3.20b}$$

Finally, using the identity $\exp[2i\pi N] = 1$ for integer N and Eqs. (3.20) and (3.18), and neglecting terms $O(\epsilon^2)$, we obtain:

$$\left[i\left(K/\beta - \Omega^2\right) + \Lambda\right](1 - \epsilon\Omega)\,\epsilon T/2 + i(\delta\omega_\pi + \Omega)T = 2i\pi N_P + \epsilon J_P, \tag{3.21a}$$

$$\left[i\left(K/\beta - \Omega^2\right) - \Lambda\right](1 + \epsilon\Omega)\,\epsilon T/2 + i(\delta\omega_\pi - \Omega)T = 2i\pi N_M + \epsilon J_M, \tag{3.21b}$$

where $N_{P,M}$ are some integer numbers and $\delta\omega_\pi$ is "the fractional part" of ω_π: If $\omega_\pi = 2\pi n/T$ (where n is not necessarily an integer) and N_π is the integer part of n, then $\delta\omega_\pi \equiv 2\pi(n - N_\pi)/T$. Note that $\delta\omega_\pi = O(1/T)$.

We can now justify neglecting the terms $O(\epsilon^2)$ in (3.14) and in subsequent calculations. Indeed, if such terms had been retained, they would have contributed amounts $O(\epsilon^2)$ and $O(\epsilon^2\Omega \cdot \epsilon T)$ to (3.21). The former amount would be a higher-order contribution than that provided by terms $\epsilon J_{P,M}$, which we need to determine. The latter amount, strictly speaking, depends on the order of magnitude of (ϵT), but it will be clear from our subsequent calculations that even terms $O(\epsilon\Omega \cdot \epsilon T)$ can be neglected in the leading-order analysis.

Step 4: Completing the analysis using the results of Steps 2 and 3.

We will now use Eqs. (3.19) and (3.21) to determine for what values of Ω the instability increment $\beta\Lambda_R$ is nonzero. To this end, we first subtract Eqs. (3.21) from each other and take the real part, obtaining:

$$\Lambda_R = \frac{\mathrm{Re}(J_P - J_M)}{T}. \tag{3.22}$$

Next, adding Eqs. (3.21) one obtains:

$$\epsilon(J_P + J_M) = \left(iK/\beta - i\Omega^2 - \Lambda\,\epsilon\Omega\right)\epsilon T + 2i\delta\omega_\pi T - 2i\pi(N_P + N_M). \tag{3.23}$$

Using Eq. (3.22) one notices that the real part of the the r.h.s. of (3.23) is of order $O(\epsilon^2)$ and hence should be neglected. Thus we conclude that in the main order, $(J_P + J_M)$ is purely imaginary. For future use, we also display the result of taking the imaginary part of the difference of the two equations (3.21):

$$\mathrm{Im}(J_P - J_M) = \left(-\left(K/\beta - \Omega^2\right)\epsilon\Omega + \Lambda_I\right)\epsilon T + 2\Omega T - 2\pi(N_P - N_M). \tag{3.24}$$

Since Λ_R is proportional to the real part of $(J_P - J_M)$, we solve for the latter quantity using Eqs. (3.19). To that end, we first solve for R by adding these equations and then substitute the answer in their difference, obtaining:

$$J_P - J_M = \pm\frac{i\gamma}{\beta}\sqrt{\left(2\mathcal{F}[U^2](0) + i(\beta/\gamma)(J_P + J_M)\right)^2 - \left|\mathcal{F}[U^2](2\Omega)\right|^2}. \tag{3.25}$$

Now recall that, as noted after (3.23), $(J_P + J_M)$ is purely imaginary. Also, $\mathcal{F}[U^2](0)$ is real. Then the real part of the r.h.s. of (3.25) is nonzero when

$$-\left|\mathcal{F}[U^2](2\Omega)\right| \;\leq\; 2\mathcal{F}[U^2](0) + i(\beta/\gamma)(J_P + J_M) \;\leq\; \left|\mathcal{F}[U^2](2\Omega)\right|. \qquad (3.26)$$

Under this condition, one also has

$$\mathrm{Im}(J_P - J_M) = 0. \qquad (3.27)$$

Thus, the instability increment, $\beta\Lambda_R$, is found from Eqs. (3.22) and (3.25), where $(J_P + J_M)$ is determined from (3.23). The last two equations, in their turn, involve three yet undetermined quantities: Ω, which labels the frequency of an unstable Fourier mode, parameter Λ_I introduced in (3.10), and $(N_P + N_M)$. We will now show that within the accuracy adopted in our calculations, the former two quantities enter all equations in a unique combination $(\Omega + \epsilon\Lambda_I/2)$, and hence the number of yet undetermined quantities reduces to two. Indeed, upon substitution of (3.15) into (3.10), we observe that *up to terms $O(\epsilon^2)$*, both t- and z-dependences of p and m involve Ω and Λ_I only in the aforementioned combination $(\Omega + \epsilon\Lambda_I/2)$. Next, by inspection of formulae (3.23) and (3.24), one can easily see that, within the same accuracy, they also involve Ω and Λ_I only in that combination. This means that one can set $\Lambda_I = 0$. Then from (3.24) and (3.27) one finds:

$$\Omega = \pi(N_P - N_M)/T, \qquad (3.28)$$

where we have discarded terms $O(\epsilon^2)$. Then (3.23) is rewritten as

$$i(J_P + J_M) = -\left(\frac{K}{\beta} + \frac{2\delta\omega_\pi}{\epsilon}\right)T + \left(\frac{\pi^2(N_P - N_M)^2}{T} + \frac{2\pi(N_P + N_M)}{\epsilon}\right). \qquad (3.29)$$

Finally, one substitutes the last two equations into (3.26) and determines those values of $(N_P \pm N_M)$ where the instability can occur. The instability increment is computed from (3.22) and (3.25), and the frequency of the unstable mode, from (3.28). Examples of such a calculation, producing the theoretical results shown in Figs. 3 and 4, are given in Section 4.2. $\square$

Comment: The main difference between the von Neumann and present analyses.

In the standard von Neumann analysis, an instability can be found by expanding the numerical error in a set of Fourier harmonics that are purely oscillatory in the spatial coordinate. In contrast, the unstable harmonics in the above analysis exhibit slow exponential growth or decay in the spatial variable t: see (3.10) and (3.15) and note that for those harmonics, $\Lambda_R \neq 0$. Purely oscillatory harmonics do *not* become unstable on the soliton's background.

The exponentially growing or decaying spatial harmonics in (3.15) are also different from those required for the standard numerical stability analysis of initial-boundary-value problems (see, e.g., [10]). The latter harmonics decay *rapidly* away from the

17

boundary, so that they do not "see" the other boundary of the spatial domain. In other words, the standard analysis of stability of initial-boundary-value problems is *local* to each point of the boundary of the spatial domain [10]. In contrast, the exponentially growing or decaying harmonics in (3.15) are *not local* to each boundary since they must satisfy periodic boundary conditions. What allows those spatially growing or decaying modes to satisfy periodic boundary conditions is the jump that they undergo on the soliton; see (3.17) and (3.20). This is also shown schematically in Fig. 6 for a mode in the $p \exp[-i\omega_\pi t]$-wave.
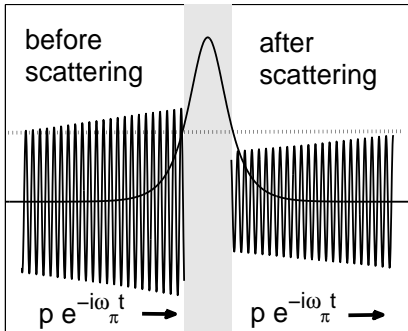

Figure 6: A schematics showing that in order to satisfy periodic boundary conditions, a mode that changes its amplitude due to scattering on the soliton *must* be spatially growing or decaying rather than purely oscillatory.

In Appendices 2 and 3 we present related technical results. Namely, in Appendix 2 we show that if one seeks unstable modes not specifically near $\pm\omega_\pi$, as we did at the beginning of this subsection, but instead near an arbitrary pair of frequencies $\pm\omega_0$, one discovers that the instability can arise only near $\pm\omega_\pi$, $\pm\omega_{2\pi}$, etc. In Appendix 3 we modify the analysis of this subsection to apply to a monochromatic-wave background (1.4) and thereby recover results that can be deduced from those obtained by Weideman and Herbst [6].

4   Validation of the theory

In the first subsection below, we will give qualitative explanations of the instability features described in Section 2: the locations and widths of the instability peaks, and high sensitivity of the instability to the step size, the time window length T, and the shape of the background solution. In the second subsection, we will work out an example showing how Eqs. (3.22), (3.25), (3.26), (3.29), and (3.28) were used to compute the increment and frequency of the unstable Fourier modes reported in Figs. 3

18

and 4. We will conclude by generalizing the order-of-magnitude estimate (3.11) for the unstable modes' separation frequency, 2Ω.

4.1 Qualitative explanation of instability features reported in Section 2

The results of Section 3.2 allow us to explain why the instability peaks, shown in Fig. 2, are not reflectionally symmetric about $\omega = 0$ (see the paragraph after Eq. (2.2)). Indeed, from Eqs. (3.8), (3.10), and (3.15), one sees that the frequencies of two coupled unstable modes are

$$\big(\omega_\pi + \Omega - \epsilon(-K/\beta + \Omega^2)/2\big) \qquad \text{and} \qquad -\big(\omega_\pi - \Omega - \epsilon(-K/\beta + \Omega^2)/2\big). \qquad (4.1)$$

Thus, given the sign difference of the second terms inside the parentheses above, the mode at $\omega_{\text{right}}^{(+)}$ is coupled to the mode at $\omega_{\text{right}}^{(-)}$ and *not* to that at $\omega_{\text{left}}^{(-)}$, as it would have been in the case of reflectional symmetry.

Similarly, two other features of the instability spectra reported in Section 2 can also be explained. First, note from (3.28) and (3.29) that if a value $\Omega > 0$ is found to correspond to an instability peak, then so is $-\Omega < 0$. This observation, along with relations

$$\omega_{\text{right}}^{(\pm)} = \pm\big(\big[\omega_\pi - \epsilon(-K/\beta + \Omega^2)/2\big] \pm \Omega\big) \qquad \text{and} \qquad \omega_{\text{left}}^{(\pm)} = \pm\big(\big[\omega_\pi - \epsilon(-K/\beta + \Omega^2)/2\big] \mp \Omega\big),$$
$$(4.2)$$

which follow from (4.1), explains why relations (2.3) hold. Second, the slight asymmetry of the frequencies $\omega_{\text{right}}^{(\pm)}$ and $\omega_{\text{left}}^{(\pm)}$ about the respective $\pm\omega_\pi$, is also easily explained. Indeed, the frequencies of, say, the peaks at $\omega_{\text{right}}^{(+)}$ and $\omega_{\text{left}}^{(+)}$, as seen from (4.2), are centered about $\big[\omega_\pi - \epsilon(-K/\beta + \Omega^2)/2\big]$ and *not* about ω_π. The magnitude of the shift, $-\epsilon(-K/\beta + \Omega^2)/2$, agrees with the numerically observed values. For example, in the experiments reported in Table 1, $K = 1$, $\beta = -1$, $\epsilon \sim 0.04$, and $\Omega \sim 0.5$, and hence $-\epsilon(-K/\beta + \Omega^2)/2 \sim -0.025$. This should be compared to the experimental values of $\big[(\omega_{\text{left}}^{(+)} - \omega_\pi) + (\omega_{\text{right}}^{(+)} - \omega_\pi)\big]/2$, which from Table 1 are seen to vary between -0.02 and -0.03 [2].

Next, we can explain why in most cases, as mentioned in Sections 2 and 3.1, the instability peaks contain just one node[3]. Consider Eqs. (3.28) and (3.29) and assume that at frequency labeled by Ω_0, corresponding to a particular $(N_P - N_M)_0$, there is an instability. The frequency at the adjacent node differs from this Ω_0 by $2\pi/T$, and

---

[2] A more detailed comparison would require keeping at least one more significant digit in the data of Table 1, but such a comparison does not appear to be needed. Rather, it is the quantitative agreement of our theory and numerical experiments, reported in Figs. 3 and 4 and presented in the next subsection, which seems to be the most important test confirming the validity of the theory.

[3] As we already mentioned in Section 2, the pedestals around the peaks arise due to a non-numerical — modulational — instability, and those pedestals are hence unrelated to the foregoing explanation.

hence, according to (3.28), the corresponding $(N_P - N_M)$ differs from $(N_P - N_M)_0$ by 2. Consistently with this, one can take $(N_P + N_M) = (N_P + N_M)_0$. Then the corresponding value of the r.h.s. of (3.29) differs from that value at Ω_0 by $2\pi^2(N_P - N_M)_0/T \cdot 2 = 4\pi\Omega_0$. On the other hand, the interval of values where $i(J_P + J_M)$ corresponds to an instability is found from (3.26) to have the width $2\left|(\gamma/\beta)\mathcal{F}[U^2](2\Omega_0)\right|$. Thus, whenever

$$4\pi\Omega > 2\left|(\gamma/\beta)\mathcal{F}[U^2](2\Omega)\right|, \tag{4.3}$$

the instability peak can contain only one node. Using expression (1.8) for $U(t)$, one finds that condition (4.3) holds for $\Omega > 0.46$. In other words, it is only when the peaks at ω_{left} and ω_{right} are separated by less than 0.92 that they can contain more than one node. In practice, the separation should be even smaller, given a random location of the node with the unstable frequency within the instability interval. In fact, among the simulations reported in Section 2, we observed multiple nodes per peak only when $(\omega_{\text{right}} - \omega_{\text{left}})$ was about 0.25 or less.

The high sensitivity of the instability to the length T of the time window, which was highlighted in Section 2 (see also Table 2 there), is also easily explained using (3.29). Suppose this length is changed from T_0 to T, so that the relative change $(T - T_0)/T_0$ is small. Then the r.h.s. of (3.29) is changed by an amount

$$-\left(\frac{2\delta\omega_\pi}{\epsilon} + \Omega^2\right) \cdot T_0 \cdot \frac{T - T_0}{T_0} \ . \tag{4.4}$$

The coefficient in front of $(T - T_0)/T_0$ is large due to T_0 being large and the terms in parentheses being $O(1)$. Note that this does not necessarily imply that the instability will disappear, since new values of N_P and N_M may exist for which the r.h.s. of (3.29) will be inside the instability interval (3.26); see the next subsection for a quantitative example in a similar situation where not T but Δz, is varied.

Similarly, the high sensitivity of the instability to the soliton's amplitude A occurs because $K \equiv A^2$ on the r.h.s. of (3.29) is multiplied by a large parameter T.

Finally, while instability on the background of several well-separated solitons cannot be computed from Eqs. (3.25) and (3.26), which were obtained for a single soliton, one can still explain why the instability is sensitive to the number of the solitons and their relative locations. Indeed, the number of solitons determines the number of jumps in the "slow" variables P and M; see (3.16)–(3.19). Its is those jumps that allow modes that exponentially grow/decay (in t) away from the jumps to exist in the presence of periodic boundary conditions in t; see (3.21). And its is those modes, exponentially growing or decaying (as opposed to purely oscillating) *in t*, that are also exponentially growing (i.e., are unstable), in the evolution variable z; note the same exponent Λ in (3.15) and in (3.10). As for the relative locations of the solitons, they (as well as the solitons' phases) determine the counterparts of parameter R in a generalization of Eqs. (3.19) for a multi-soliton background.

4.2 Example of calculation of instability increment and frequency

Here we will explain in detail how the instability increment and frequency for the generic case are found. Such a generic case corresponds to, e.g., $\Delta z = 0.0043$ in Fig. 3, for which we will present the calculations below. Its instability spectrum is qualitatively the same as that shown in Fig. 2. Then we will comment on less common cases, whose spectra are shown in Fig. 5. We will conclude this section by establishing a general dependence of Ω as a function of ϵ and T.

For all cases considered here, the parameters in the background soliton (1.8) are: $\beta = -1$, $\gamma = 2$, $A = 1$, whence $K = 1$ and $U(t) = \text{sech}(t)$. The time window is $T = 128\pi$ and the number of grid points is 2^{12}. These are the same parameters as were used in obtaining Figs. 3 – 5.

To begin, let us recall from (3.25) and (3.26) that for the mode labeled by Ω to be unstable, the left-hand side (l.h.s.) of (3.29) must fall within the interval

$$\left(4\mathcal{F}[U^2](0) - 2\left|\mathcal{F}[U^2](2\Omega)\right|, \ \ 4\mathcal{F}[U^2](0) + 2\left|\mathcal{F}[U^2](2\Omega)\right| \right) \tag{4.5}$$

(here we have used that $\gamma/\beta = -2$). While Ω is yet undetermined and hence $\left|\mathcal{F}[U^2](2\Omega)\right|$ is not known exactly, it cannot exceed $\mathcal{F}[U^2](0) = 2$, and hence interval (4.5) is always inside the interval (4, 12). Thus, this interval contains values of order 1, i.e. much smaller than any of the terms on the r.h.s. of (3.29), which are proportional to the large parameters T and $1/\epsilon = \omega_\pi$. This observation motivates our strategy of finding suitable values of $(N_P \pm N_M)$.

First, given the above values of parameters, one finds $\omega_\pi = 1/\epsilon \approx 27.03$, $\delta\omega_\pi \approx 0.0140$, and then the first term on the r.h.s. of (3.29):

$$-\left(\frac{K}{\beta} + \frac{2\delta\omega_\pi}{\epsilon}\right) T \approx 96.86 \,. \tag{4.6}$$

Next, since the first term in the second parentheses, $(\pi(N_P - N_M))^2/T$, is always positive, we seek such an integer value for $(N_P + N_M)$ that an expression

$$-\left(\frac{K}{\beta} + \frac{2\delta\omega_\pi}{\epsilon}\right) T + \frac{2\pi(N_P + N_M)}{\epsilon} \tag{4.7}$$

is as close to zero as possible but negative[4]. Since $2\pi/\epsilon \approx 169.84$, the corresponding $N_P + N_M = -1$, yielding the value of -72.98 for (4.7). Finally, an integer value of $(N_P - N_M)$ is sought to make the value of the r.h.s. of (3.26) fit within the interval (4.5). To this end, one first *estimates* $(N_P - N_M)$ by forcing that r.h.s. to equal zero:

$$(N_P - N_M)_{\text{estimated}} = \sqrt{\frac{T}{\pi^2}\left[\left(\frac{K}{\beta} + \frac{2\delta\omega_\pi}{\epsilon}\right) T - \frac{2\pi(N_P + N_M)}{\epsilon}\right]} \,. \tag{4.8}$$

---

[4]Modifications of this requirement will give rise to "less common" cases, considered later.

Here $(N_P - N_M)_{\text{estimated}}$ is not an integer; e.g., for the example above it is approximately 54.53. Then a nearby integer value for $(N_P - N_M)$ is found by trial and error so that it makes the r.h.s. of (3.29) fit within the interval (4.5) (see a clarification in the next paragraph). For the above example, this value is $(N_P - N_M) = 57$, yielding $\Omega \approx 0.45$ (see (3.28)). Substitution of this value into (3.25) and (3.22) yields $\beta\Lambda_R = 0.0066$. Comparison of so computed $\beta\Lambda_R = \text{Re}(\lambda)$ and $\Omega = (\omega_{\text{right}} - \omega_{\text{left}})/2$ (see (4.2)) with respective values found numerically is shown in Figs. 3 and 4 for various values of Δz.

Two notes are in order about the last step described above. First, since both N_P and N_M are integers, then $(N_P + N_M)$ and $(N_P - N_M)$ are either both odd or both even. Second, once a guess is made about $(N_P - N_M)$, then Ω is computed from (3.28) and hence $\left|\mathcal{F}[U^2](2\Omega)\right|$ in (4.5) and (3.25) is found from (1.3). A Matlab code that facilitates the calculations presented above can be found at

`http://www.cems.uvm.edu/~lakobati/posted_papers_and_codes/2010_splitstep`.

We will now briefly describe what we have referred to above as "less common" cases, depicted in Fig. 5. Let us first address the situation depicted in Fig. 5a, which occurs for, e.g., $\Delta z = 0.0044, 0.0045, 0.00474, 0.0049$. The inner pair of instability peaks is found in these cases as described above. For example, for $\Delta z = 0.0049$, it is obtained using $(N_P + N_M) = -2$ and $(N_P - N_M) = 62$. The corresponding calculated instability increment and the peak separation are $\beta\Lambda_R \approx 0.0051$ and $2\Omega \approx 2 \cdot 0.48$, which are very close to the experimentally observed values. However, if for the same value of Δz one takes $(N_P + N_M) = -3$, then one finds that an instability can exist at $\Omega \approx 0.78$, corresponding to $(N_P - N_M) = 101$. The calculated and observed values of the instability increment for this outer pair of peaks are 0.0030 and 0.0039, respectively.

Let us note that we checked — by trial and error, as described in the previous paragraph — for the existence of a secondary pair of instability peaks for every value of Δz reported in Figs. 3 and 4. For each Δz where such a secondary pair was observed in numerics, we also found it analytically, with the agreement between the calculated and observed values of Ω being excellent and those of Λ_R being good (the discrepancy between such values for $\Delta z = 0.0049$, reported above, was the worst one we found). We even found, both numerically and analytically, small tertiary peaks for $\Delta z = 0.0044$. On the other hand, we *analytically* found secondary peaks for $\Delta z = 0.0042, 0.00475, 0.00477$ where they were not observed in numerics at $z = z_{\text{max}} = 2000$. However, at smaller z, such secondary peaks were indeed observed. The reason they were not observed for $z = 2000$ was that they were "drowned" by the pedestal of unstable modes which "rose" around the primary peaks due to modulational — i.e., non-numerical — instability about the primary peaks.

We will now comment on the calculation of the central peak for the case of $\Delta z = 0.0050$, shown in Fig. 5b. Here the value of (4.7) with $(N_P + N_M) = -1$ is approximately 11.1. This is not negative, as we wanted this expression to be in the previous calculations (see the line after (4.7)). However, for $(N_P - N_M) = 0$, the r.h.s. of (3.29)

22

is 11.1 ∈ (4, 12), i.e. it is within the instability interval (4.5) with $\Omega = 0$ (see (3.28)). According to the discussion found around Eq. (4.3), the instability peak at $\Omega = 0$ should contain several grid nodes, which is confirmed by Fig. 5b.

Finally, let us revisit the estimate for the order of magnitude of Ω, which determines the frequency separation of the primary instability peaks. In (3.11) we stated, as an empirical observation, that $\Omega = O(1)$. We will now use Eq. (4.8) to generalize it. Note that for the largest integer value of $(N_P + N_M)$ that still renders expression (4.7) negative, the expression in the square brackets in (4.8) is no greater than $2\pi \cdot 1/\epsilon$. The corresponding $(N_P - N_M)_{\text{estimated}}$, and hence $(N_P - N_M)$, is then of the order $O(\sqrt{T/\epsilon})$. Substitution of this into (3.28) yields

$$\Omega = O(1/\sqrt{\epsilon T}). \tag{4.9}$$

Thus, as one makes the time window wider in the order-of-magnitude sense while keeping the other parameters fixed, the separation between the primary unstable Fourier modes should, *on average*, descrease. An implication of this for observing the numerical instability is presented in Section 6.

5 Instability of higher-order split-step methods

It is well-known (see, e.g., [11]) that method (1.2) has first-order accuracy in Δz. Its single step can be symbolically written as

$$u_{n+1} = e^{\Delta z \mathcal{L}} e^{\Delta z \mathcal{N}} u_n, \tag{5.1}$$

where $\exp[\Delta z \mathcal{N}]$ and $\exp[\Delta z \mathcal{L}]$ are the symbols denoting, respectively, evolutions due to only the nonlinear and only the linear (i.e., dispersive) terms in Eq. (1.1). The two second-order split-step methods (see, e.g., [1, 11]),

$$u_{n+1} = e^{\Delta z/2\,\mathcal{L}} e^{\Delta z \mathcal{N}} e^{\Delta z/2\,\mathcal{L}} u_n, \qquad u_{n+1} = e^{\Delta z/2\,\mathcal{N}} e^{\Delta z \mathcal{L}} e^{\Delta z/2\,\mathcal{N}} u_n, \tag{5.2}$$

are equivalent to method (5.1) except for their first and last half-steps. Hence the stability properties of methods (5.2) and (5.1) are the same. Below we will focus on two fourth-order versions of the split-step method:

$$u_{n+1}^{(I)} = e^{c_1 \Delta z \mathcal{L}} e^{d_1 \Delta z \mathcal{N}} e^{c_2 \Delta z \mathcal{L}} e^{d_2 \Delta z \mathcal{N}} e^{c_2 \Delta z \mathcal{L}} e^{d_1 \Delta z \mathcal{N}} e^{c_1 \Delta z \mathcal{L}} u_n^{(I)}, \tag{5.3a}$$

$$u_{n+1}^{(II)} = e^{c_1 \Delta z \mathcal{N}} e^{d_1 \Delta z \mathcal{L}} e^{c_2 \Delta z \mathcal{N}} e^{d_2 \Delta z \mathcal{L}} e^{c_2 \Delta z \mathcal{N}} e^{d_1 \Delta z \mathcal{L}} e^{c_1 \Delta z \mathcal{N}} u_n^{(II)}, \tag{5.3b}$$

where [12, 11]

$$c_1 = \frac{1}{2(2 - 2^{1/3})}, \quad c_2 = (1 - 2^{1/3})c_1, \quad d_1 = 2c_1, \quad d_2 = -2^{1/3}d_1. \tag{5.4a}$$

Note that
$$2c_1 + 2c_2 = 1, \qquad 2d_1 + d_2 = 1. \tag{5.4b}$$

Starting with method (5.3a), we note that its stability properties are equivalent to those of the method
$$u_{(i)} = e^{c_2 \Delta z \mathcal{L}} e^{d_1 \Delta z \mathcal{N}} u_n, \tag{5.5a}$$
$$u_{(ii)} = e^{c_2 \Delta z \mathcal{L}} e^{d_2 \Delta z \mathcal{N}} u_{(i)}, \tag{5.5b}$$
$$u_{n+1} = e^{2c_1 \Delta z \mathcal{L}} e^{d_1 \Delta z \mathcal{N}} u_{(ii)}, \tag{5.5c}$$

where we have omitted the superscipt '(I)' for brevity. In analogy with Eq. (3.3), the linearized form of Eq. (5.5a) can be written as:

$$\mathcal{F}[\tilde{u}_{(i)}] = e^{i\beta\omega^2(c_2\Delta z)} \mathcal{F}\left[\tilde{u}_n + i\gamma(d_1\Delta z)(u_{\text{sol}}^2\tilde{u}_n^* + 2|u_{\text{sol}}|^2\tilde{u}_n)\right]. \tag{5.6}$$

As in Appendix 2, one can show that the numerical instability can occur only near the frequencies $\pm\omega_\pi$, $\pm\omega_{2\pi}$, etc. Below we will focus on the vicinity of $\omega = \omega_\pi$, whence

$$\beta\omega^2 c_2\Delta z = c_2(\beta\omega_\pi^2\Delta z) + \beta(\omega^2 - \omega_\pi^2)c_2\Delta z = -c_2\pi + O(\epsilon), \tag{5.7}$$

where we have used (1.6) with $\beta < 0$ and the argument found after (3.4). Substituting (5.7) into (5.6) and its complex conjugate and proceeding as explained after (3.6), we obtain:

$$\begin{pmatrix} \tilde{u}_{(i)} \\ \tilde{u}_{(i)}^* \end{pmatrix} = \Phi_2 \, \mathcal{E}_{d_1, c_2} \begin{pmatrix} \tilde{u}_n \\ \tilde{u}_n^* \end{pmatrix}, \tag{5.8}$$

where

$$\Phi_j = \begin{pmatrix} e^{i\phi_j} & 0 \\ 0 & e^{-i\phi_j} \end{pmatrix}, \qquad \phi_j = -c_j\pi, \qquad j = 1, 2; \tag{5.9}$$

$$\mathcal{E}_{d, c} = \begin{pmatrix} e^{-i\beta(c\Delta z)(\omega_\pi^2 + \partial_t^2)} & 0 \\ 0 & e^{i\beta(c\Delta z)(\omega_\pi^2 + \partial_t^2)} \end{pmatrix} \begin{pmatrix} 1 + i\gamma(d\Delta z)\cdot 2|u_{\text{sol}}^2| & i\gamma(d\Delta z)\cdot u_{\text{sol}}^2 \\ -i\gamma(d\Delta z)\cdot(u_{\text{sol}}^*)^2 & 1 - i\gamma(d\Delta z)\cdot 2|u_{\text{sol}}^2| \end{pmatrix}. \tag{5.10}$$

Similarly,

$$\begin{pmatrix} \tilde{u}_{(ii)} \\ \tilde{u}_{(ii)}^* \end{pmatrix} = \Phi_2 \, \mathcal{E}_{d_2, c_2} \begin{pmatrix} \tilde{u}_{(i)} \\ \tilde{u}_{(i)}^* \end{pmatrix}, \qquad \begin{pmatrix} \tilde{u}_{n+1} \\ \tilde{u}_{n+1}^* \end{pmatrix} = \Phi_1^2 \, \mathcal{E}_{d_1, 2c_1} \begin{pmatrix} \tilde{u}_{(ii)} \\ \tilde{u}_{(ii)}^* \end{pmatrix}. \tag{5.11}$$

Combining (5.8) and (5.11), one has:

$$\begin{pmatrix} \tilde{u}_{n+1} \\ \tilde{u}_{n+1}^* \end{pmatrix} = \Phi_1^2 \, \mathcal{E}_{d_1, 2c_1} \Phi_2 \, \mathcal{E}_{d_2, c_2} \Phi_2 \, \mathcal{E}_{d_1, c_2} \begin{pmatrix} \tilde{u}_n \\ \tilde{u}_n^* \end{pmatrix}. \tag{5.12}$$

If matrices $\Phi_{1,2}$ commuted with $\mathcal{E}_{d,c}$'s, then (5.12) *would have become*

$$\begin{pmatrix} \tilde{u}_{n+1} \\ \tilde{u}_{n+1}^* \end{pmatrix} = \Phi_1^2 \, \Phi_2^2 \, \mathcal{E}_{d_1, 2c_1} \mathcal{E}_{d_2, c_2} \mathcal{E}_{d_1, c_2} \begin{pmatrix} \tilde{u}_n \\ \tilde{u}_n^* \end{pmatrix}. \tag{5.13}$$

24

But (5.13) is equivalent to (3.4) and hence to (3.7) by the following arguments. First,

$$\Phi_1^2 \, \Phi_2^2 \;=\; \begin{pmatrix} -1 & 0 \\ 0 & -1 \end{pmatrix} \tag{5.14}$$

by virtue of (5.9) and the first equation in (5.4b). Second, the action of operator $\mathcal{E}_{d_1,\,2c_1}\mathcal{E}_{d_2,\,c_2}\mathcal{E}_{d_1,\,c_2}$ is analogous to the action of the operator on the r.h.s. of (3.6) (except that the former operator approximates the differential equation (A1.2) with a higher accuracy). Then, *if* (5.13) *were true*, it would have reduced to (A1.2) and hence to (3.7). This would have implied that the instability of the higher-order split-step methods were identical to the instability of the lower-order method (1.2). However, (5.13) *is not true* because matrices Φ and $\mathcal{E}$ do *not* commute. For this reason, the instability of the higher-order methods (5.3) is *different* from that of method (1.2).

Below we will derive an equation that is, up to terms $O(\epsilon)$, equivalent to (5.12) and which therefore becomes a counterpart of (3.7) for the higher-order method (5.3a). Having derived that equation, (5.21) below, we will point out how the analysis of Section 3 can be applied to it in a straightforward manner.

First, we note that

$$\mathcal{E}_{d,\,c}\Phi_j \;=\; \Phi_j \, \mathcal{E}_{d,\,c} + \mathcal{C}_{d,\,c;\,\phi_j}\,, \tag{5.15a}$$

$$\mathcal{C}_{d,\,c;\,\phi_j} = \begin{pmatrix} 0 & 2\gamma u_{\text{sol}}^2 \cdot (d\Delta z)\sin\phi_j \\ 2\gamma (u_{\text{sol}}^*)^2 \cdot (d\Delta z)\sin\phi_j & 0 \end{pmatrix} + O(\epsilon). \tag{5.15b}$$

(Recall that $|\omega^2 - \omega_\pi^2|\Delta z = O(\epsilon) = O(\sqrt{\Delta z})$.) Then (5.12) becomes:

$$\begin{pmatrix} \tilde{u}_{n+1} \\ \tilde{u}_{n+1}^* \end{pmatrix} = \left[\Phi_1^2 \, \Phi_2^2 \, \mathcal{E}_{d_1,\,2c_1}\mathcal{E}_{d_2,\,c_2}\mathcal{E}_{d_1,\,c_2} + \Phi_1^2 \left(\mathcal{C}_{d_1,\,2c_1;\,2\phi_2}\mathcal{E}_{d_2,\,c_2} + \mathcal{E}_{d_1,\,2c_1}\Phi_2\mathcal{C}_{d_2,\,c_2;\,\phi_2} \right) \mathcal{E}_{d_1,\,c_2} \right] \begin{pmatrix} \tilde{u}_n \\ \tilde{u}_n^* \end{pmatrix}. \tag{5.16}$$

Next, an easy calculation shows that

$$\mathcal{C}_{a,\,b;\,\phi}\,\mathcal{E}_{c,\,d} = \mathcal{C}_{a,\,b;\,\phi} + O(\Delta z \cdot \epsilon), \qquad \mathcal{E}_{c,\,d}\,\mathcal{C}_{a,\,b;\,\phi} = \mathcal{C}_{a,\,b;\,\phi} + O(\Delta z \cdot \epsilon). \tag{5.17}$$

Using (5.17), (5.15b), and (5.14), we transform (5.16) into

$$\begin{pmatrix} \tilde{u}_{n+1} \\ \tilde{u}_{n+1}^* \end{pmatrix} = \left[-\mathcal{E}_{d_1,\,2c_1}\mathcal{E}_{d_2,\,c_2}\mathcal{E}_{d_1,\,c_2} + \begin{pmatrix} 0 & f \\ f^* & 0 \end{pmatrix} + O(\Delta z \cdot \epsilon) \right] \begin{pmatrix} \tilde{u}_n \\ \tilde{u}_n^* \end{pmatrix}, \tag{5.18a}$$

$$f = 2\gamma u_{\text{sol}}^2 \Delta z\, e^{2i\phi_1} \left(d_1 \sin(2\phi_2) + d_2 e^{i\phi_2}\sin\phi_2 \right). \tag{5.18b}$$

As explained after (5.14), it is the second term on the r.h.s. of (5.18a) that makes the instability of method (5.3a) different from the instability of method (1.2).

Now, note that the off-diagonal entries of the first term on the r.h.s. of (5.18a) are:

$$\left(-\mathcal{E}_{d_1,\,2c_1}\mathcal{E}_{d_2,\,c_2}\mathcal{E}_{d_1,\,c_2} \right)_{\text{off-diag}} = - \begin{pmatrix} \cdots & g \\ g^* & \cdots \end{pmatrix} + O(\Delta z \cdot \epsilon), \tag{5.19a}$$

25

$$g = i\gamma \Delta z u_{\mathrm{sol}}^2. \tag{5.19b}$$

(That is, g is the coefficient multiplying $\tilde{u}_n^*$ in (3.4).) This follows by the same argument as used after Eq. (5.14). Combining (5.18) and (5.19) and discarding the $O(\Delta z \cdot \epsilon)$ terms, we obtain that

$$\begin{array}{c} \text{operator on} \\ \text{r.h.s. of (5.18a)} \end{array} = - \left[(\mathcal{E}_{d_1,\,2c_1} \mathcal{E}_{d_2,\,c_2} \mathcal{E}_{d_1,\,c_2})_{\mathrm{diag}} + \begin{pmatrix} \cdots & g - f \\ (g-f)^* & \cdots \end{pmatrix} \right]. \tag{5.20}$$

Note that g and f differ only by a constant factor. Then it follows from (5.20) that in the leading order, the entire second term on the r.h.s. of (5.16) affects *only the coefficient* of the off-diagonal entries. This, in turn, means that (5.12) reduces, via (5.16) and the arguments found after (3.4) and (3.6), to the following *modification of (3.7)*:

$$\tilde{w}_z = -i\beta(\tilde{w}_{tt} + \omega_\pi^2 \tilde{w}) - iK\tilde{w} + i\gamma U^2 \left(\sigma \tilde{w}^* + 2\tilde{w} \right), \tag{5.21}$$

where, as follows from (5.20), (5.19b), and (5.18b),

$$\sigma \equiv \sigma^{(I)} = 1 + 2i\, e^{2i\phi_1} \left(d_1 \sin(2\phi_2) + d_2 e^{i\phi_2} \sin \phi_2 \right). \tag{5.22}$$

(Here we have restored the superscript '(I)', thus indicating that (5.21) and (5.22) describe the instability of the first of the fourth-order accurate split-step methods, (5.3a).) An analysis of Eq. (5.21) follows precisely the lines of Section 3.2, with the only difference being that the quantity $|\mathcal{F}[U^2](2\Omega)|$ in (3.25), (3.26), and (4.5) is now multiplied by $|\sigma^{(I)}|$. Numerical results validating this conclusion are presented at the end of this section.

The instability analysis for the other higher-order method, (5.3b), is done similarly. Namely, the counterpart of (5.12) is now

$$\begin{pmatrix} \tilde{u}_{n+1} \\ \tilde{u}_{n+1}^* \end{pmatrix} = \Psi_1 \, \mathcal{E}_{c_2,\,d_2} \Psi_2 \, \mathcal{E}_{c_2,\,d_1} \Psi_1 \, \mathcal{E}_{2c_1,\,d_1} \begin{pmatrix} \tilde{u}_n \\ \tilde{u}_n^* \end{pmatrix}, \tag{5.23}$$

where

$$\Psi_j = \begin{pmatrix} e^{i\psi_j} & 0 \\ 0 & e^{-i\psi_j} \end{pmatrix}, \qquad \psi_j = -d_j \pi, \qquad j = 1, 2. \tag{5.24}$$

Then, following the derivations found between Eqs. (5.15) and (5.20), one finds that the corresponding modification of Eq. (3.7) has the form (5.21) with σ being replaced by

$$\sigma \equiv \sigma^{(II)} = 1 + 2ic_2\, e^{i\psi_1} \left(\sin(\psi_1 + \psi_2) + e^{i\psi_2} \sin \psi_1 \right). \tag{5.25}$$

From (5.4), (5.9), and (5.24) one finds:

$$|\sigma^{(I)}| \approx 0.4847, \qquad |\sigma^{(II)}| \approx 1.5598, \tag{5.26}$$
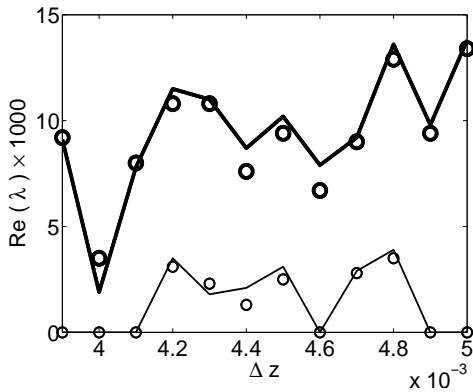
Figure 7: Instability increment as a function of the step size Δz, obtained for the same parameters as in Fig. 3a, but for methods (5.3a) (thin line and circles) and (5.3b) (thick line and circles). The locations of the unstable peaks are the same as in Fig. 3b (see text).

A comparison of the theoretical results based on the analysis of Eqs. (5.21), (5.22), and (5.25) with the results of numerical simulations is shown in Fig. 7. A few remarks about it are in order.

First, the theoretical values of the instability increment are computed as explained in Section 4.2; see also the end of the paragraph following Eq. (5.22). The parameters of numerical simulations are the same as for Figs. 3 and 4, with one minor exception. Namely, the simulations for the two most unstable cases, with $\Delta z = 0.0048$ and 0.0050 for method (5.3b), were run up to only $z_{\max} = 1000$, because running them up to $z_{\max} = 2000$ created a conspicuous distortion of the background soliton.

Second, (5.26) shows that $|\sigma^{(I)}| < 1 < |\sigma^{(II)}|$. This fact along with the analysis of Section 3.2 implies that the instability for method (5.3b) should be, on average, stronger and also observed more often than the instability for method (1.2). The latter, in turn, should be stronger and observed more often than the instability for method (5.3a). Both these conclusions are confirmed by Fig. 7. Let us also note that the fact that the instabilities on the monochromatic-wave background are different for methods (5.3a) and (5.3b) was demonstrated (by the von Neumann analysis) in [8], although no connection to Eq. (5.21) was made there.

Third, it is clear from Section 4.2 that the *location* of unstable Fourier harmonics, i.e., parameter Ω, is not affected by the coefficient of $|\mathcal{F}[U^2](2\Omega)|$. Therefore, the location of the unstable peaks for methods (5.3) *is the same* as that for method (1.2). This is confirmed by our numerics. An exception is the instability at $\Delta z = 0.0040$, which is absent for methods (1.2) and (5.3a) but appears for method (5.3b). There, we also confirmed that the theoretical and numerical values of the unstable peaks' locations are in excellent agreement (as in Figs. 3b and 4b).

27

Fourth and last, it should be noted that method (5.3a) is "less unstable" than method (5.3b) near $\omega = \pm\omega_\pi$, but *not* near *all* resonant frequencies $\omega_{m\pi}$, $m = 1, 2, 3, \ldots$. In fact, a calculation based on (5.9) and (5.24) where π is replaced by 2π reveals that *near $\omega = \pm\omega_{2\pi}$*,

$$|\sigma^{(I)}| \approx 3.3074, \qquad |\sigma^{(II)}| \approx 1.4547, \tag{5.27}$$

i.e. there, method (5.3a) is "more unstable" than both methods (5.3b) and (1.2).

6   Conclusions

We reported, and then analytically explained, a numerical instability in the split-step Fourier method (1.2) applied to the nonlinear Schrödinger equation (1.1) with the background solution being the soliton (1.8). Properties of this instability, such as the dependence of its increment and unstable mode's location on the step size, numerical domain's length T, and details of the background solution, are quite different from those properties on the background of the monochromatic wave (1.4), previously obtained by the von Neumann analysis in [6]. Namely, the dependence of the instability on those parameters is seemingly very irregular, as we illustrated in Tables 1, 2 and Figs. 3, 4. This is to be contrasted with monotonic dependences of the numerical instability observed for finite-difference schemes in both constant- and variable-coefficients equations, as described in textbooks on numerical methods. Moreover, we demonstrated (see the end of Section 2) that the principle of "frozen coefficients" is not valid for the split-step Fourier method on the background of a localized nonlinear wave. In particular, the instabilities on the background of a single soliton, on one hand, and several well-separated identical solitons, on the other, can be drastically different.

The analysis presented in Section 3 (see also Appendix 2) revealed that unstable modes can be found only near the resonant frequencies $\pm\omega_\pi$, $\pm\omega_{2\pi}$, etc. (see (1.6) and the sentence after that equation). Remarkably, far away from the soliton, these unstable modes are *not* exactly periodic in the spatial variable t. Rather, their spatial envelope is exponentially growing or decaying in t (see Eqs. (3.8), (3.10), (3.15), and (3.22)). What makes these modes satisfy the periodic boundary conditions, which are implicitly imposed by the use of Fourier transform in (1.2), is the change that they undergo near the soliton. Thus, *the finite size of the numerical domain T is critical in our instability analysis*, which is in stark contrast with the standard von Neumann analysis.

In Section 5 we extended the analysis of Section 3 to higher-order split-step methods, such as (5.3).

As we noted above, the dependence of the instability increment on the parameters of the soliton and the numerical scheme is irregular, and there is no means to predict it "quickly", i.e., bypassing the procedure illustrated in Section 4.2. Again, this

is in contrast with the instability analysis on a monochromatic-wave background [6] (see [8] and Appendix 3). However, one can still obtain two general conclusions: (i) what maximum value this increment can have and (ii) how the chances to observe a numerical instability depend on the size T of the numerical domain. We provide the corresponding details in the next two paragraphs for the lower-order method (1.2). These details generalize straightforwardly for the higher-order split-step methods, considered in Section 5.

The maximum instability increment is obtained from Eqs. (3.22) and (3.25) by setting $2\mathcal{F}[U^2](0) + i(\beta/\gamma)(J_P + J_M) = 0$. This yields:

$$\left(\beta\Lambda_R\right)_{\max} = \frac{1}{T}\left(\gamma\left|\mathcal{F}[U^2](2\Omega)\right|\right)_{\max} = \frac{\gamma}{T}\mathcal{F}[U^2](0) \equiv \frac{\gamma}{T}\int_{-T/2}^{T/2} U^2(t)\, dt. \qquad (6.1)$$

Interestingly, the last expression above is the same as an analogous expression in the monochromatic-background case (see Eq. (A3.5) in Appendix 3), where $U(t) \equiv A$.

Now let us show that as the time window length T is *substantially* decreased, the chances to observe numerical instability in any given simulation using (1.2) with (2.1), also decrease[5]. This conclusion follows from a combination of arguments that led to formulae (4.3) and (4.9). Indeed, recall from a discussion after Eq. (4.8) that an instability would arise only if near the non-integer number $(N_P - N_M)_{\text{estimated}}$, there is an integer number $(N_P - N_M)$ that would make the r.h.s. of (3.29) fit within the interval (4.5). A sufficient condition that would guarantee that such an $(N_P - N_M)$ can be found is obtained similarly to (4.3):

$$4\pi\Omega_{\text{estimated}} < 2\left|(\gamma/\beta)\mathcal{F}[U^2](2\Omega_{\text{estimated}})\right|, \qquad (6.2)$$

where $\Omega_{\text{estimated}} \equiv \pi(N_P - N_M)_{\text{estimated}}/T$. As follows from the discussion around (4.9), $\Omega_{\text{estimated}} = O(1/\sqrt{\epsilon T})$. Thus, as T decreases, the chances that condition (6.2) may be satisfied, also decrease. Hence the smaller T is, the "less often" a numerical instability of scheme (1.2) on the background of a soliton would be observed. On the other hand, the smaller T is, the stronger the numerical instability, if it *is* observed, is on average; this follows from (6.1). Both these conclusions agree with our observations in Section 2: Compare Table 1, obtained for $T = 32\pi$, with Fig. 3, obtained for $T = 128\pi$.

Finally, let us point out that the analysis of this paper can be straightforwardly generalized to any scalar equation of the form

$$u_t = \mathcal{L}[u] + \mathcal{N}[u], \qquad (6.3)$$

where the linear, $\mathcal{L}$, and nonlinear, $\mathcal{N}$, "parts" of the evolution are solved exactly in the split-step method. However, certain other generalizations, e.g., (i) for vector

---

[5]Note the word 'substantially'. As illustrated by Table 2 in Section 2, changing T by only a *small* fraction of its value affects the occurrence of the instability in a non-monotonic and seemingly irregular way.

equations where the Fourier transform of $\mathcal{L}[u]$ is not proportional to the identity matrix, or (ii) for the case when $\mathcal{L}[u]$ is solved by a finite-difference method with non-periodic boundary conditions, require further investigation.

Acknowledgement

Appendix 1: Derivation of Eq. (3.7)

We verified that one can derive (3.7) from (3.6) by using a Taylor series expansion of $\exp[i\beta(\omega^2 - \omega_\pi^2)\Delta z]$ and $(\tilde{v}_{n+1} - \tilde{v}_n)$ in powers of ϵ. However, an alternative derivation presented below is much less tedious and, importantly, more intuitive.

Let us first note that the last equation in (1.2) is equivalent to the nonlinear Schrödinger equation (1.1) *plus* a term proportional to

$$\Delta z \beta \gamma \cdot [\partial_{tt}, |u(t,z)|^2]u(t,z) + O(\Delta z^2), \tag{A1.1}$$

where $[\ldots, \ldots]$ denotes a commutator. This follows from the Baker–Campbell–Hausdorff formula; see, e.g., Sec. 2.4.1 in [1]. Next, Eq. (3.3) is a linearized version of the last equation in (1.2). Therefore, it must be equivalent to the linearized nonlinear Schrödinger equation plus terms of order $O(\beta \Delta z \partial_{tt}) = O(\beta \omega^2 \Delta z) = O(\epsilon^2)$, provided that we assume that $\omega \sim \partial_t = O(1)$, or, equivalently, that the central frequency in expanding $\exp[i\beta\omega^2\Delta z]$ in a Taylor series is 0.

In writing (3.4) and then (3.6), we stated that the central frequency is ω_π (or $-\omega_\pi$) rather than 0. Correspondingly, Eq. (3.6) must be equivalent to a *modified* linearized nonlinear Schrödinger equation written for a small deviation $\tilde{v}$, plus terms of order $O\big(\beta(\omega^2 - \omega_\pi^2)\Delta z\big) = O(\epsilon)$ (see the text after (3.4)). Here the modification consists in replacing the operator ∂_{tt}, whose Fourier symbol is $-\omega^2 \equiv -(\omega^2 - 0^2)$, with the operator $\partial_{tt} + \omega_\pi^2$, whose Fourier symbol is $-(\omega^2 - \omega_\pi^2)$. Thus, (3.6) in the time domain is

$$\tilde{v}_z = -i\beta(\tilde{v}_{tt} + \omega_\pi^2 \tilde{v}) + i\gamma(u_{\text{sol}}^2 \tilde{v}^* + 2|u_{\text{sol}}|^2\tilde{v}) + O(\epsilon). \tag{A1.2}$$

Substituting into this equation u_{sol} from (1.8), changing the variable $\tilde{v} = \tilde{w}\exp[iKz]$, and neglecting the $O(\epsilon)$ term, one obtains Eq. (3.7).

Appendix 2: Location of instability peaks

Here we will present an explaination of why the frequencies of unstable modes must be near $\pm\omega_\pi$, $\pm\omega_{2\pi}$, etc.

Suppose we seek the instability near a pair of frequencies $\pm\omega_0$; i.e., we assume that

$$|\omega - \omega_0| = O(1) \qquad \text{or} \qquad |\omega - (-\omega_0)| = O(1) \,. \qquad (A2.1)$$

Then, proceeding as explained in the text after Eq. (3.3), we obtain an equation similar to (3.4), where the "(-1)" and ω_π on the r.h.s. are replaced with $\exp[i\phi_0]$ and ω_0, respectively, where

$$\phi_0 = \beta\omega_0^2\Delta z \,. \qquad (A2.2)$$

Then (3.5) and (3.6) get replaced with

$$\tilde{v}_n = e^{-i\phi_0 n}\,\tilde{u}_n \,, \qquad (A2.3)$$

$$\mathcal{F}[\tilde{v}_{n+1}] = e^{i\beta(\omega^2-\omega_0^2)\Delta z}\,\mathcal{F}\left[\tilde{v}_n + i\gamma\Delta z(u_{\text{sol}}^2\tilde{v}_n^* \cdot \underline{e^{-2i\phi_0 n}} + 2|u_{\text{sol}}|^2\tilde{v}_n)\right]\,, \qquad (A2.4)$$

where the term making the key difference between (3.6) and (A2.4) is underlined. Let us now note that if the phase rotation per step, $-2\phi_0$, in that term would equal $-2\pi N$, where N is any integer, then that term would equal 1, and the subsequent analysis would proceed as in Section 3.2 without any changes. Therefore, we can say that the *nontrivial* phase rotation in (A2.4) is $-(2\phi_0 - 2\pi N_0)$, where N_0 is the nearest integer to ϕ_0/π. For simplicity, but without loss of generality, let us assume that $N_0 = 1$; the case of $N_0 \neq 1$ is completely analogous. Then, Eq. (A2.4) becomes

$$\mathcal{F}[\tilde{v}_{n+1}] = e^{i\beta(\omega^2-\omega_0^2)\Delta z}\,\mathcal{F}\left[\tilde{v}_n + i\gamma\Delta z\big(u_{\text{sol}}^2\tilde{v}_n^* e^{-2i\beta(\omega_0^2-\omega_\pi^2)n\Delta z} + 2|u_{\text{sol}}|^2\tilde{v}_n\big)\right]\,, \qquad (A2.5)$$

where in rewriting the exponential term we have used (A2.2) and (1.6).

To go from the discrete equation (A2.5) to a counterpart of the continuous equation (3.7), we make two observations. First, $n\Delta z = z$ in the second exponential term in (A2.5). Second, and perhaps counter-intuitively: Despite the presence of this possibly fast-oscillating exponential, Eq. (A2.5) still describes a *small* change for $(\tilde{v}_{n+1} - \tilde{v}_n)$. This is due to the presence of the small terms $i\gamma\Delta z$ and $\beta(\omega^2 - \omega_0^2)\Delta z$ (see (A2.1)) on the r.h.s. of that equation. Therefore, the continuous variable $\tilde{v}(t, z)$ interpolating the discrete variable in (A2.5) satisfies a counterpart of (A1.2):

$$\tilde{v}_z = -i\beta(\tilde{v}_{tt} + \omega_0^2\tilde{v}) + i\gamma\big(u_{\text{sol}}^2\tilde{v}^* e^{-2i\beta(\omega_0^2-\omega_\pi^2)z} + 2|u_{\text{sol}}|^2\tilde{v}\big) + O(\epsilon)\,. \qquad (A2.6)$$

In analogy with the argument presented in Appendix 1, we make a change of variables

$$\tilde{v} = \tilde{w}\,\exp\left[i(K - \beta(\omega_0^2 - \omega_\pi^2))z\right]\,, \qquad (A2.7)$$

which transforms (A2.6) into the following counterpart of (3.7):

$$\tilde{w}_z = -i\beta(\tilde{w}_{tt} + \omega_0^2\tilde{w}) - i\big(K - \beta(\omega_0^2 - \omega_\pi^2)\big)\tilde{w} + i\gamma U^2(\tilde{w}^* + 2\tilde{w})\,. \qquad (A2.8)$$

Then, a substitution analogous to (3.8) with ω_π being replaced by ω_0 into Eq. (A2.8) yields a system of equations that is similar to (3.9), with the only changes being the replacements:

$$\omega_\pi \quad \text{by} \quad \omega_0 \qquad \text{and} \qquad K \quad \text{by} \quad (K - \beta(\omega_0^2 - \omega_\pi^2))\,. \qquad (A2.9)$$

We now need to consider two cases: (i) $\beta(\omega_0^2 - \omega_\pi^2) = O(1)$ and (ii) $|\beta(\omega_0^2 - \omega_\pi^2)| \gg 1$. We will show that in the first case, the results of analysis of Eqs. (3.9) with replacements (A2.9) reduce to those obtained in Section 3.2, and in the second case, no instability can arise.

In case (i), $\omega_0 - \omega_\pi = O(\epsilon)$, i.e. this case differs from that considered in Section 3.2 only by a slight shift of the central frequency. Intuitively, such a shift could not change the location of the unstable peaks which we found to be away from ω_π by an amount of approximately $\Omega = O(1)$. Formally, this can be justified by a tedious calculation that reveals that Eqs. (3.28), (3.29) with replacements (A2.9) yield the same Ω as the original Eqs. (3.28), (3.29). Then, Eqs. (3.10), (3.15) with replacements (A2.9) yield the same t-dependence of the solution of (3.8) as the original Eqs. (3.10), (3.15). Thus, in case (i), the parameters of the instability reduce to those found in Section 3.2.

In case (ii), one cannot proceed as in case (i) by merely using replacements (A2.9) in Eqs. (3.9). The reason is that $\left|K - \beta(\omega_0^2 - \omega_\pi^2)\right| \gg 1$, whereas in case (i) one had $\left(K - \beta(\omega_0^2 - \omega_\pi^2)\right) = O(1)$. Indeed, in case (ii), a substitution (3.10) with $\Omega = O(1)$ (which is our starting assumption — see (A2.1)) would not yield p_{slow} and m_{slow} that would be slow functions of t; see the first term on the r.h.s. of (3.14). The only way the large term $\left(K - \beta(\omega_0^2 - \omega_\pi^2)\right)$ could be eliminated from the couterpart of (3.9) is by using *different* z-dependences in the exponentials in (3.10):

$$p = p_{\text{slow}}(\tau, z) \exp\left[-i\Omega t + 2i(\beta/\epsilon)\Omega z + \beta\Lambda z - i\left(K - \beta(\omega_0^2 - \omega_\pi^2)\right)z\right], \quad \text{(A2.10a)}$$

$$m = m_{\text{slow}}(\tau, z) \exp\left[i\Omega t + 2i(\beta/\epsilon)\Omega z + \beta\Lambda z + i\left(K - \beta(\omega_0^2 - \omega_\pi^2)\right)z\right]. \quad \text{(A2.10b)}$$

(Note that the last terms in the exponents in (A2.10) essentially undo transformation (A2.7).) In (A2.10), p_{slow} and m_{slow} are slow functions of t, but not of z. Substituting (A2.10) into the counterpart of (3.9) one would obtain, instead of the z-independent system (3.14), a z-dependent system of the form:

$$(p_{\text{slow}})_z = b_{11}(p_{\text{slow}})_\tau + b_{12}p_{\text{slow}} + b_{13}\, m_{\text{slow}}\, e^{2i\left(K - \beta(\omega_0^2 - \omega_\pi^2)\right)z}, \quad \text{(A2.11a)}$$

$$(m_{\text{slow}})_z = b_{21}(m_{\text{slow}})_\tau + b_{22}m_{\text{slow}} + b_{23}\, p_{\text{slow}}\, e^{-2i\left(K - \beta(\omega_0^2 - \omega_\pi^2)\right)z}, \quad \text{(A2.11b)}$$

where all the coefficients b_{ij} are of order $O(1)$ and independent of z. The presence of rapidly oscillating exponential terms in (A2.11) makes the effect of the coupling terms negligible, and then system (A2.11) gets essentially decoupled into two independent equations for p_{slow} and m_{slow}, which does not exhibit any instability. Thus, in case (ii) numerical instability does not occur.

Appendix 3: Instability on the background of a monochromatic wave

Here we will use the method presented in Section 3.2 to find the location and growth rate of the numerically unstable Fourier modes of method (1.2) on the background of a monochromatic wave (1.4) with $\Omega_{\mathrm{cw}} = 0$. Let us note that these results can be obtained from formulae (65), (37), and (64) of [6] by expanding them in a power series of the step size Δz (denoted there by τ). In such a way, the growth rate of the most unstable mode was obtained in [8].

The starting point of our derivation is system (3.9), which holds both for the soliton and monochromatic-wave backgrounds. In the latter case, $U(t) \equiv A$ and $K = \gamma A^2$, where without loss of generality we assume that A is real. Thus, now this system, unlike (3.9) on the soliton background, has *all constant* coefficients, and hence we can look for its solution in the form

$$\{p, m\} = \{P, M\} e^{iW\epsilon t + \lambda z}, \qquad W = O(1). \tag{A3.1}$$

Note that unlike in (3.10), here the p- and m-components of the small deviation $\tilde{w}$ have the same t-dependence. Also, we have used the notation W, not Ω, in (A3.1), because, unlike Ω, the variable W does not have the dimension of frequency. Rather, $\epsilon W \equiv W/\omega_\pi$ has the same dimension as Ω.

Substitution of (A3.1) into (3.9) with the aforementioned values of U and K yields:

$$(2i\beta W - i\gamma A^2 + \lambda) P - i\gamma A^2 M = 0, \tag{A3.2a}$$

$$-i\gamma A^2 P + (2i\beta W - i\gamma A^2 - \lambda) M = 0, \tag{A3.2b}$$

where we have neglected terms $O(\epsilon^2)$. Then the instability growth rate is

$$\lambda = \sqrt{(\gamma A^2)^2 - (2\beta W - \gamma A^2)^2}. \tag{A3.3}$$

The location of the unstable mode(s) follows from the definition of the mode's frequency, $\omega = \omega_\pi - \epsilon W \equiv \omega_\pi - (W/\omega_\pi)$, and the condition that the expression under the radical in (A3.3) is positive:

$$0 < \beta W < \gamma A^2. \tag{A3.4}$$

The maximum value of the growth rate occurs at the midpoint of this interval and is

$$\lambda_{\max} = \gamma A^2. \tag{A3.5}$$

Note that the periodicity condition for p and m does *not* play here a critical role in determining the instability increment, in stark contrast to the case of the soliton background considered in Section 3.2. Namely, as follows from (3.8) and (A3.1), here this condition simply requires that the frequency $\omega = \omega_\pi - \epsilon W$ fall onto the frequency

grid: $\omega_\pi - \epsilon W = 2\pi\ell/T$, where ℓ is an integer. Thus, if the width of the instability band is less than the frequency grid spacing:

$$\gamma A^2/(|\beta|\omega_\pi) < 2\pi/T, \qquad (A3.6)$$

it is possible that $2\pi\ell/T$ may fall outside the instability band. In this case, the instability will not occur even if Δz exceeds the threshold (1.7). This was originally pointed out by Weideman and Herbst [6] and studied in detail by Yang in [8].

Generalization of the above derivations for the higher-order split-step methods, considered in Section 5, is straightforward.

References

[1] G.P. Agrawal, Nonlinear fiber optics, 3rd Ed., Academic Press, San Diego, 2001.

[2] R.H. Hardin, F.D. Tappert, Applications of the split-step Fourier method to the numerical soltion of nonlinear and variable coefficient wave equations, SIAM Review (Chronicle) 15 (1973), 423.

[3] A. Hasegawa, F. Tappert, Transmission of stationary nonlinear optical pulses in dispersive dielectric fibers. I. Anomalous dispersion, Appl. Phys. Lett. 23 (1973), 142–144.

[4] R.A. Fisher, W. Bischel, The role of linear dispersion in plane-wave self-phase modulation, Appl. Phys. Lett. 23 (1973), 661–663.

[5] T. Taha, M. Ablowitz, Analytical and numerical aspects of certain nonlinear evolution equations. II. Numerical, Nonlinear Schrodinger equation, J. Comp. Phys. 55 (1984), 203–230.

[6] J.A.C. Weideman, B.M. Herbst, Split-step methods for the solution of the non-linear Schrödinger equation, SIAM J. Numer. Anal. 23 (1986), 485–507.

[7] F. Matera, A. Mecozzi, M. Romagnoli, M. Settembre, Sideband instability induced by periodic power variation in long-distance fiber links, Opt. Lett. 18 (1993), 1499–1501.

[8] J. Yang, Nonlinear waves in integrable and non-integrable systems, SIAM, Philadelphia (to appear); Sec. 7.1.

[9] J. VonNeumann, R.D. Richtmeyer, A method for the numerical calculation of hydrodynamic shocks, J. Appl. Phys. 21 (1950), 232–237.

[10] J.C. Strikwerda, Finite-difference schemes for partial-differential equations, 2nd Ed., SIAM, Philadelphia, 2004; Chap. 11.

[11] H. Yoshida, Construction of higher order symplectic integrators, Phys. Lett. A 150 (1990), 262–268.

[12] F. Neri, Lie algebras and canonical integration, Department of Physics, University of Maryland, preprint (1987).

List of Figure captions

1. Schematics of the numerical instability increment of method (1.2) over the background of a monocromatic wave (1.4) as a function of frequency ω. Only the part for $\omega > 0$ is shown, since the graph is symmetric about $\omega = 0$. The width of the instability peak near $\omega_{k\pi}$, where $k = 1, 2, \ldots$, equals $|\gamma A^2/(\beta \omega_{k\pi})|$ (see Appendix 3). Note that the case corresponding to $\beta < 0$ is shown; in the case of $\beta > 0$, the peaks will occur on the opposite sides of ω_π and $\omega_{2\pi}$.

2. The spectrum of the solution of (1.1) and (2.1) at $z = 500$ with $\Delta z = 0.0040$, computed by method (1.2). Other parameters are listed in the text after Eq. (2.1).

3. Instability increment and unstable peaks' half-separation at $z = 2000$, as a function of the step size Δz. The initial condition is (2.1). The numerical domain has length $T = 128\pi$ and contains 2^{12} grid points. Note that for $\Delta z = 0.0040$, where no instability is found, we *defined* the corresponding $\omega_{\text{right}} - \omega_{\text{left}} = 0$.

4. Same as in Fig. 3, but for a different interval of Δz values.

5. "Less typical" instability spectra. Both panels are for initial condition (2.1), the propagation distance $z = 2000$, and the numerical domain with $T = 128\pi$ and 2^{12} grid points. (a) $\Delta z = 0.0049$; similar spectra are found for $\Delta z = 0.0044, 0.0045, 0.00474$; (b) $\Delta z = 0.0050$.

6. A schematics showing that in order to satisfy periodic boundary conditions, a mode that changes its amplitude due to scattering on the soliton *must* be spatially growing or decaying rather than purely oscillatory.

7. Instability increment as a function of the step size Δz, obtained for the same parameters as in Fig. 3a, but for methods (5.3a) (thin line and circles) and (5.3b) (thick line and circles). The locations of the unstable peaks are the same as in Fig. 3b (see text).

Table 1

Δz	$\omega_{\text{left}}^{(+)} - \omega_\pi$	ω_π	$\omega_{\text{right}}^{(+)} - \omega_\pi$	$\text{Re}(\lambda)$
0.0040	-0.72	28.03	0.66	0.019
0.0048	-0.39	25.58	0.35	0.031
0.0054	-0.62	24.12	0.57	0.022
0.0055	-0.52	23.90	0.48	0.024
0.0058	-0.46	23.27	0.42	0.022

Table 1: Parameters of the unstable frequencies' peaks when $T = 32\pi$, number of grid points is 2^{10}, and Δz is varied as 0.0040, 0.0041, 0.0042, ... , 0.0060. The notations $\omega_{\text{right, left}}^{(+)}$ are introduced in Fig. 2.

Table 2

T	$\omega_{\text{left}}^{(+)} - \omega_\pi$	$\omega_{\text{right}}^{(+)} - \omega_\pi$	$\text{Re}(\lambda)$
397	-0.44	0.40	0.0062
398	-0.10	0.08	0.0096
399	-1.09	1.02	0.0024
400	-0.33	0.29	0.0076
128π	-0.39	0.36	0.0076

Table 2: Parameters of the unstable frequencies' peaks when $\Delta z = 0.0043$ ($\omega_\pi = 27.03$), number of grid points is 2^{12}, and T is varied.